THE SEASONALITY OF AEROSOL PROPERTIES IN BIG BEND NATIONAL PARK

A Thesis

by

CHRISTOPHER LEE ALLEN

Submitted to the Office of Graduate Studies of
Texas A&M University
in partial fulfillment of the requirements for the degree of

MASTER OF SCIENCE

December 2005

Major Subject: Atmospheric Sciences

THE SEASONALITY OF AEROSOL PROPERTIES IN

BIG BEND NATIONAL PARK

A Thesis

by

CHRISTOPHER LEE ALLEN

Submitted to the Office of Graduate Studies of
Texas A&M University
in partial fulfillment of the requirements for the degree of

MASTER OF SCIENCE

Approved by:

Chair of Committee,	Don R. Collins
Committee Members,	William H. Marlow
	Sarah D. Brooks
Head of Department,	Richard E. Orville

December 2005

Major Subject: Atmospheric Sciences

ABSTRACT

The Seasonality of Aerosol Properties in Big Bend National Park. (December 2005)

Christopher Lee Allen, B.S., Texas A&M University

Chair of Advisory Committee: Dr. Don R. Collins

Two-week sampling periods during the spring, summer, and fall of 2003, and the winter of 2004 were conducted utilizing a tandem differential mobility analyzer (TDMA) and, during the spring and summer, an aerodynamic particle sizer (APS), to characterize the seasonal variability of the Big Bend regions aerosol optical properties. Mass extinction efficiencies and relative humidity scattering enhancement factors were calculated for both externally and internally mixed aerosol populations for all size distributions collected, in an effort to possibly improve upon the default EPA mass extinction efficiencies used for all Class 1 areas across the United States. The mass extinction efficiencies calculated differed to some extent form the default values employed by the EPA. Sulfate, nitrate, and light absorbing carbon (LAC) exhibited a strong dependence on assumed mixing state, while, additionally, sulfate was also dependent on the assumed dominant aerosol. Seasonal variability was seen with all particle types, excluding LAC, with sulfate mass extinction efficiencies displaying the greatest variability with season. Calculated back trajectories indicated that air masses originating from the southeast had elevated mass extinction efficiencies, while, conversely, air masses originating from the southwest and northwest had the smallest mass extinction efficiencies.

ACKNOWLEDGEMENTS

I truly feel privileged to have numerous people in my life that warrant my acknowledgement. First and foremost I would like to thank my chair, Dr. Don Collins, for supporting and believing in me and introducing me to atmospheric chemistry; without this chance I would not be here today. I would like to thank Dr. Runjun Li and Chance Spencer for helping me quickly adjust to all aspects lab and instrumentation, and Dr. Roberto Gasparini for all his guidance with any and all aspects of field and lab research. I would like to recognize Dr. Gary Sickler for the motivation he provided me to attend graduate school.

From a personal standpoint my family has always been a vital piece of my life. My parents John and Debby, siblings Melanie and Elizabeth have always provided me with what I needed to succeed, without them I would not be were I am today. I wish to thank my father and mother-in-law, Greg and Janet Eastin and my sister-in-law Amy Eastin; they have been extremely supportive during the past few years. I would like to acknowledge my many cohorts in mischief over the years, Colin Linerode, Robert Grady, Benji Chen, Jimmy Martin, Justin Fentress, and Jeremy Tusant, whom many nights of craziness helped me keep my sanity. I would especially like to thank my wife, soul mate, and best friend Rebecca Allen. To all that truly know, she is my better half and has given me so many wonderful memories and moments. Of course this would all be futile without God. It's through his unconditional love and his eternal peace that all of this is possible.

TABLE OF CONTENTS

Page

LIST OF FIGURES

Page

Page

LIST OF TABLES

Page

CHAPTER I

INTRODUCTION

Anthropogenic aerosols in remote regions are gaining far greater interest because of their adverse effects on not only human and animal health but also the deteriorating visibility in many remote regions. There have been numerous studies throughout the past decade focusing on aerosol physical and optical properties in an attempt to curb many of the adverse effects aerosols cause (Brown et. al., 2002; Day et. al., 2000; Dick et. al., 2000; Malm and Day, 2000; Zhang et. al., 1993). An area of increased notoriety is Big Bend National Park located along the Texas-Mexico border in remote western Texas. Regions like the Big Bend area of Texas have become the focus of increased public concern for the past decade because of the degraded visibility, the worst of any national park or wildlife area (Class 1 area) in the western US (Eldred et al., 1987; Malm et al., 1990, 1994; Sisler et al., 1993, 1996), inhibiting the region's magnificent natural beauty. In 1999 the Environmental Protection Agency (EPA) enacted legislation known as The Regional Haze Rule to improve air quality in all Class 1 areas throughout the US, strengthening the 1977 Clean Air Act. The legislation enacted requires states and federal agencies to work together to improve visibility in these protected areas, through the use of various field projects carried out by different state and government entities

---

This thesis follows the style of Atmospheric Environment.

and by utilizing a network of monitoring stations under the guidance of the Interagency Monitoring of Protected Visual Environments (IMPROVE) to characterize the aerosol properties in each Class 1 area.

In the summer of 1996 a multi-national field study was conducted between the United States and Mexico by the National Parks Service (NPS) and the Procuraduria Federal de Protection al Ambiente (PROFEPA) respectively. The study consisted of sites positioned in a grid on both sides of the Texas-Mexico border to examine the aerosol properties, visibility, and meteorology of the vast remote region. The ground breaking project between the two countries was envisioned with the goal that anything learned would help in assisting the development of any future studies that would be carried out in the region. The findings of the 1996 scoping study were consistent with those of the analysis done on the historical database. Sulfate concentrations were found to peak in the later summer and early fall (Gebhart et al., 2001) when back trajectories indicated the aerosol originated from the southeast. Measured light extinction was at a maximum for the period when sulfate dominated the aerosol composition. Soil and organic carbon (OC) were found to contribute little if any to the overall light extinction during the study. However it should be noted that sporadically during the summer smoke from biomass burning in Mexico and Central America played an important role in overall light extinction (Kreidenweis et. al., 2001; Hand et. al., 2002).

In 1999 the EPA, NPS, and Texas Commission on Environmental Quality (TCEQ) collaborated on the Big Bend Regional Aerosol and Visibility Observational (BRAVO) study. The goal of the study was to better understand the physical, chemical,

optical, and hygroscopic properties of the regional aerosol, and to more precisely determine the emissions source for all major aerosol species contributing to the region's deteriorating visibility. Unfortunately unlike the 1996 study, the EPA did not secure the support of PROFEPA, limiting the aerosol monitoring to north of the Rio Grande river. The findings from the BRAVO study were very similar to the 1996 study. Sulfate was found to be the dominate species in the PM2.5 in both summer and fall (Lowenthal et al., 2003; Lee et al., 2004). It was also shown that a large majority of the high extinction episodes were associated with an increase in sulfate concentrations. The remaining high extinction episodes were seemingly caused by dust originating from the Sahara. However, unlike the previous study, it was shown that OC had a significant contribution to the fine mass, nearly 20%, while nitrate was nearly nonexistent at 3% (Lee et. al., 2004). Organics were found to exhibit negligible hygroscopic properties during the study, with water growth associated with inorganic salts, specifically sulfates, accounting for the increase in PM2.5 light scattering (Malm et. al., 2003; Lowenthal et. al., 2003).

Great strides have been taken in understanding the regional aerosol properties. Unfortunately we are still limited in ascertaining extinction in these remote regions. The Reconstruction Equation (equation 1) must still be used in all Class 1 areas to determine aerosol extinction and track the progress of visibility within each area.

$$b_{ext} = f(RH)\alpha_{SO_4} m_{SO_4} + f(RH)\alpha_{NO_3} m_{NO_3} + \alpha_{OC} m_{OC} + \alpha_{LAC} m_{LAC} + \alpha_{Soil} m_{Soil} + \alpha_{CM} m_{CM} + b_{sg} \qquad (1)$$

The Reconstruction Equation applies for all Class 1 areas in the US. However there is some concern that the aerosol properties in Big Bend might differ sufficiently to cause

the EPA's mass extinction coefficients for the Reconstruction equation to become erroneous. The extinction calculated using the Reconstruction equation is not only dependent upon on the size distribution of the aerosol, but also on the composition of the aerosol (Sloane 1986), and on connections and associations between particles of different types that can cause the actual coefficients in each region to vary. Deviations in aerosol composition and the resulting variation in hygroscopic properties as well as any departure from the average relative humidity (RH) values used by the IMPROVE network, can lead to disproportionate variations of the relative humidity scattering enhancement factor (*f(RH)*) from the IMPROVE monthly average values. Inaccuracies in assumed EPA mass extinction efficiencies and *f(RH)* values for the Big Bend region can lead to inaccurate visibility readings required by the Regional Haze Rule. The regional variability aerosol properties and mass extinction efficiencies make it implausible to suppose that one equation would not suffice for all locations across the US for all periods throughout the year.

To gain a thorough understanding of these effects requires a detailed depiction of the chemical and physical properties of the regional aerosol. The optical properties of the aerosol, specifically aerosol scattering and extinction, can differ significantly with varying size distributions, composition and resulting hygroscopicity, and RH. Aerosol hygroscopicity must be accurately quantified because water uptake can lead to large variations in aerosol extinction. To precisely ascertain the complete picture of the aerosol properties in the Big Bend region, two-week sampling periods were completed for each season from spring of 2003 to winter of 2004.

CHAPTER II

EXPERIMENTAL BACKGROUND

The Aerosol Research Group's research at the IMPROVE site within Big Bend National Park employed a tandem differential mobility analyzer (TDMA) system coupled with a TSI model 3321 aerodynamic particle sizer (APS) to investigate aerosols with diameters from 0.01μm to 20μm. The TDMA system, schematically shown in figure 1, is used to characterize the submicron aerosol size distribution as well as the hygroscopic and volatility properties for submicron aerosols having diameters ranging from 0.01μm to 0.8μm. The TDMA system was also used to improve upon the current estimates of monthly *f(RH)* values for the region. An APS was used to determine the supermicron size distribution for aerosols having diameters ranging from 0.6μm to 20μm. Unfortunately, the APS was only available for sampling in the spring and summer periods due to scheduling conflicts with other ongoing projects.

The foundation of the TDMA system is formed by twin Aerosol Dynamic Inc. high flow DMA's (Stolzenburg, 1988). The DMA's that form the core of the TDMA system allow for operation at significantly higher flow rates than with similar commercially available counterparts. The higher flow rates permit improved counting statistics, and allow for more rapid measurements to be carried out than with other DMA systems. The TDMA system was constructed on a mobile structure allowing for easy operation, and quick in-field calibration of specific components within an air

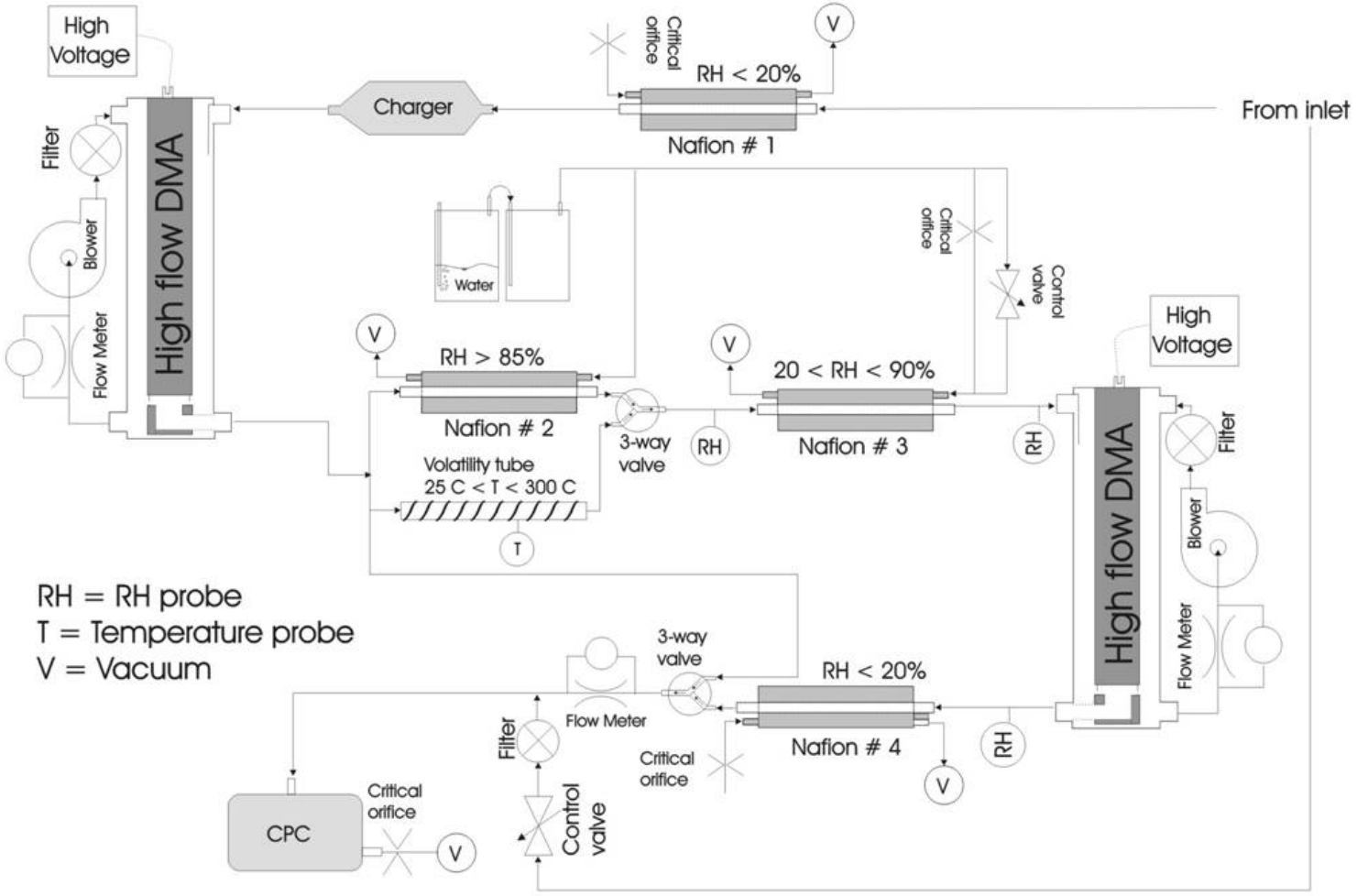

Fig. 1. Schematic of the Aerosol Research Group's TDMA system.

Fig. 2. Picture showing the air conditioned trailer used in Big Bend to house the TDMA and APS systems.

conditioned trailer shown in figure 2. Two National Instruments data acquisition cards actively control vital components of the TDMA system. The input card reads the incoming voltages from the flow meters, high voltage supplies, and RH probes. The output card supplies voltages to control the flow rates and proportional control valves through a series of Labview-based proportional-integral-differential (PID) control algorithms. A more detailed description of the individual components that make-up the TDMA system the Aerosol Research Group uses is provided in Gasparini et al. (2004).

Each DMA separates out particles in a narrow size range from the polydisperse aerosol population introduced into the system. Knutson and Whitby (1975) described a method of separating out particles by the electric mobility. This process is utilized during DMA mode, when the high voltage applied to the first DMA is varied continuously to separate aerosol particles by their electric mobility. Electric mobility (Z_p) is inversely proportional to the particle size (D_p) as shown in the following equation:

$$Z_p = \frac{neC_c}{3\pi\mu D_p} \tag{2}$$

The variable n describes the net excess or deficiency of electrons on the particle, e is the elementary unit of charge, C_C is the Cunningham correction factor, and μ is the gas viscosity. While operating the TDMA system in normal DMA mode, the second DMA is bypassed and the separated aerosols are counted by a CPC. The size-resolved aerosol concentration is determined through an inversion that accounts for the probability that a particle of given mobility will be separated out by the DMA.

The APS uniquely determines diameter by transporting aerosol particles through two laser beams and using the differential inertia of aerosol particles to count particles of different sizes. The time it takes the particle to travel from the first beam to the second beam is used to determine the diameter. The time of flight between the two laser beams is inversely proportional to D_a^2, as shown by:

$$t = \frac{18\eta L}{\rho D_a^2 a} \tag{3}$$

where L is the distance between the two laser beams, η is the viscosity of the air, D_a^2 is the aerodynamic diameter of the aerosol particle, ρ is the density of the aerosol particle, and a is the rate of acceleration of the particle. The APS operates by measuring particles of all sizes simultaneously using an integration time to achieve sufficient particle counts over the size range. The aerosol size distribution recorded by the APS is coupled with that determined with the DMA to attain a complete aerosol size distribution from 0.01μm to 20μm.

The TDMA mode is selected to determine the hygroscopic properties of the ambient aerosols. During TDMA operations particles sizes from 0.013μm to 0.6μm are logarithmically spaces and sampled successively. When operating in TDMA mode, the aerosol is directed through both DMAs. The aerosol is initially dried to an RH below 15% using a nafion bundle. The RH within the first nafion bundle is below the crystallization point for the bulk of aerosol species considered, making any remaining water content negligible. The aerosol is then introduced into the first DMA where the electric field is held constant creating a monodisperse aerosol population. The

monodisperse aerosol is then passed through a nafion bundle exposing it to an environment where the RH is maintained at 85%. Once the aerosol has passed through the humidified nafion bundle the aerosol is then introduced into the second DMA. During TDMA mode the voltage applied to the second DMA is ramped up and back down, resulting in a size-resolved hygroscopicity distribution. The particles separated out by the second DMA are then counted by the CPC using the methods previously described. The size-resolved hygroscopic aerosol distribution is described in terms of hygroscopic growth factor, the ratio of the particle following exposure to the elevated RH $\left(D_p\right)$ to its original dry diameter separated out by the first DMA $\left(D_p^*\right)$.

DMA measurements at Big Bend were made with scan times of four minutes. During the spring and summer months, TDMA scans were completed for seven sizes logarithmically spaced from 0.025μm to 0.5μm. TDMA scans made during the fall and winter sampling periods were completed for eight sizes logarithmically spaced from 0.013μm to 0.6μm. TDMA measurements completed at one particle size continued until a minimum number of particles are counted or a maximum number of scans are completed. TDMA scans times for all four sampling periods varied from two minutes to ten minutes for each particle size, depending on the relevant size-resolved concentration. Overall time for all particle sizes to be scanned averaged 60 minutes.

In addition to measuring the hygroscopicity distribution of the regional aerosol, the TDMA system is also designed to determine the deliquescence and crystallization properties of the ambient aerosol. This is done by exposing the dry monodisperse aerosol to a varying range of RH, while continuously measuring the hygroscopic growth

factor distribution. During the scans to determine the aerosol's deliquescence properties, the monodisperse aerosol separated out by the first DMA is first dried to a RH below 15% to ensure all deliquescent particles are crystalline. The crystalline monodisperse aerosol is then exposed to a higher RH, scanned by the second high flow DMA just as in TDMA mode, and then counted by the CPC. During this process the deliquescence properties of the aerosol are determined by decreasing the higher RH from roughly 90% to near 25%. The deliquescence point is identified as a discontinuity in the relationship between the hygroscopic growth factor and RH. The set of scans in which the aerosol deliquescence properties were determined will be referred to as a deliquescence scan. After the completion of the deliquescence scan, the crystallization properties of the ambient aerosol are then determined. This is done by exposing the dry monodisperse aerosol separated by the first high flow DMA to a RH above 90% to ensure all particles are hydrated. The humidified aerosol is then exposed to a lower RH, scanned by the second DMA as in TDMA mode, and counted by the CPC. The crystallization properties of the ambient aerosol are determined by increasing the lower RH from below 35% to about 90%. The crystallization point of the aerosol is the RH at the discontinuity in the relationship between the hygroscopic growth factor and RH. The set of scans in which the aerosol crystallization properties were determined will be referred to as a crystallization scan.

Lastly, to examine the volatility properties of the ambient aerosols, the aerosol is directed through a tube in which the temperature is raised initially to slightly over 300ºC. The aerosol is then continuously sampled while the temperature is allowed to cool to

ambient temperature, a process that can last as long as 60m. Following exposure to elevated temperature the aerosol is humidified in a nafion bundle to an RH of 85%. This permits independent examination of the volatility properties of the hygroscopic and non-hygroscopic aerosols. The volatility temperature of the ambient aerosol is identified by a discontinuity in the particle size and temperature relationship in a manner very similar to the determination of the crystallization and deliquescence point described previously. The volatility temperature can be used to infer the prevailing inorganic species present.

The sampling site at Big Bend was located one-quarter mile west of the IMPROVE sampling site, which lies one-half mile north of Texas Highway 118. This provided sufficient distance to minimize local contaminants from vehicle traffic. Figure 3 shows where the site was located in relation the IMPROVE site and Big Bend park headquarters, as well as Big Bend in relation to major anthropogenic sources in the region. Sampling periods were conducted at the site during April, June, and December 2003 as well as January 2004. The availability of the data from each data collection period is shown in figure 4.

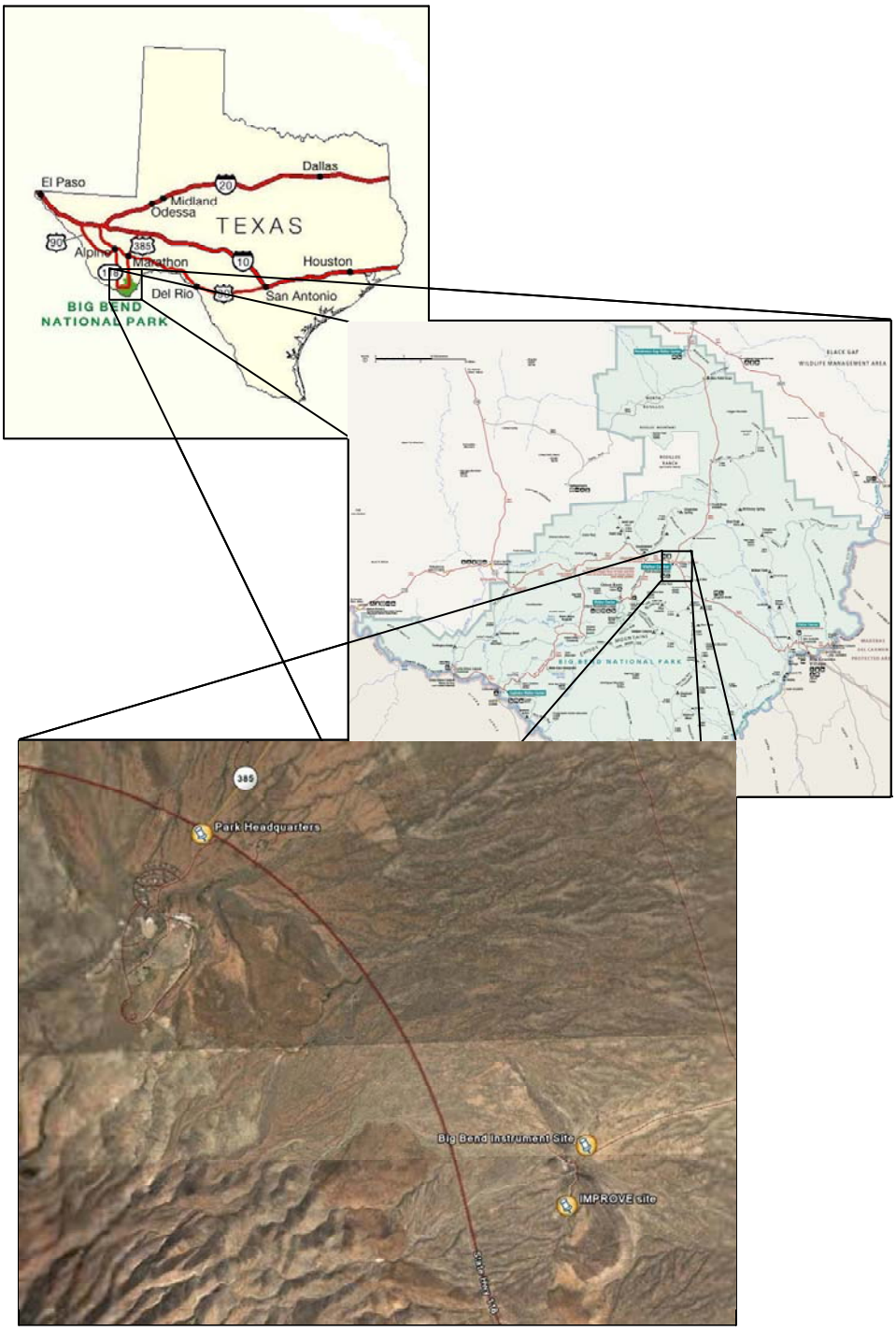

Fig. 3. Image of Big Bend's location in Texas, Map of Big Bend, and picture of the TDMA location in relation to the IMPROVE site and park headquarters.

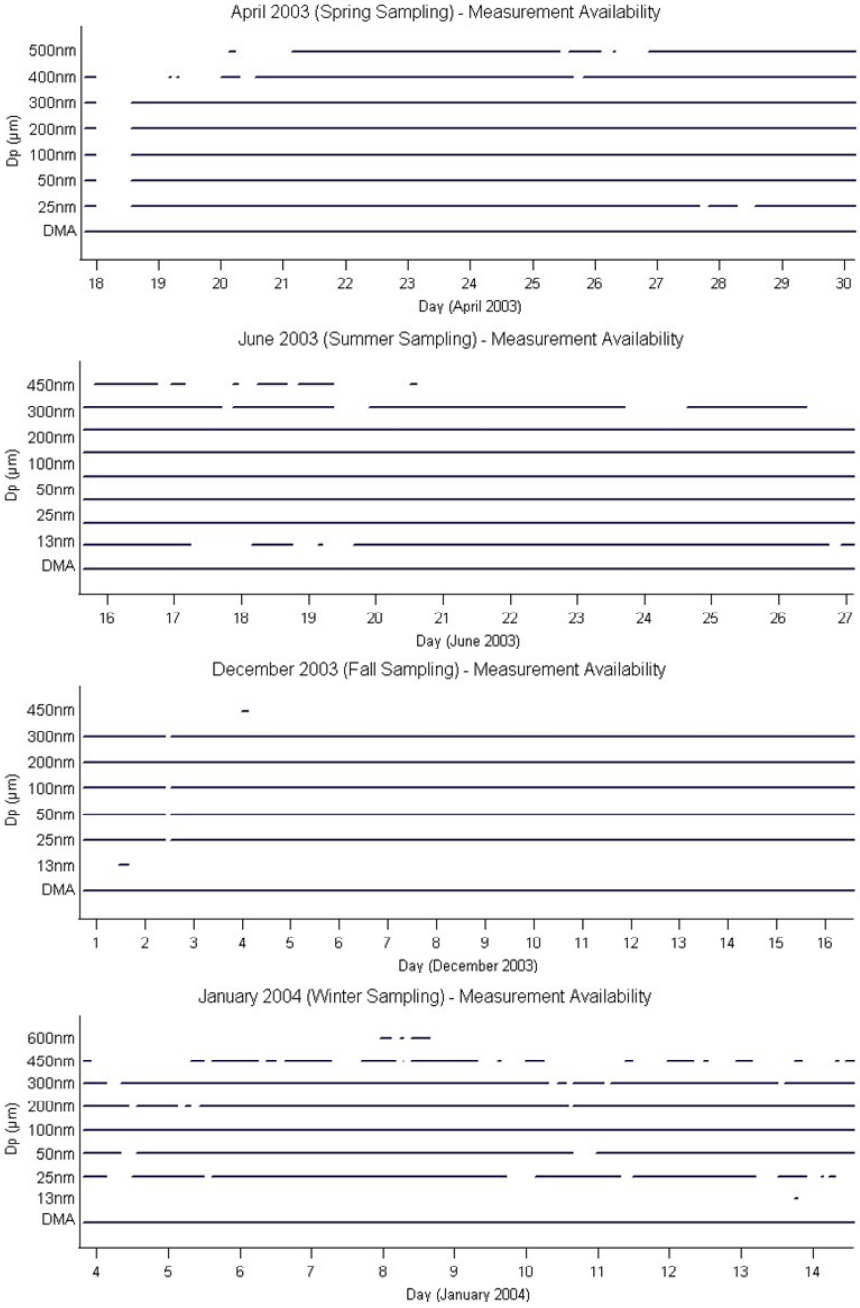

Fig. 4. Data availability for each sampling period.

CHAPTER III

ANALYSIS METHODS

The TDMA system was calibrated in lab prior to being transported to Big Bend. Components such as the flow meters and high voltage supplies drifted over a period of a few days. Full calibrations could not be accomplished in the field due to a lack of space in the trailer. In order to correct possible drifting that might occur with the flow meters and high voltage supplies, leading to erroneous hygroscopicity distributions, calibration scans were made during the first scan after midnight each day. The midnight calibration scans are composed of two different scans. During the first of these scans, the high voltages are set to zero to quantify the leak rate within the TDMA. During the second scan, the nafion tubes in the TDMA system are kept dry so that the expected growth factor of all sizes sampled should be centered at 1.0. This will be used to correct the growth factors for each size sampled due to any drifting that might have transpired in the flow meters and high voltages supplies using the following equation;

$$\beta_i^{'} = \frac{\beta_i^{*}}{\beta_i} \tag{4}$$

were $\beta_i^{'}$ is the corrected growth factor, β_i^{*} is the original measured growth factor and β_i is the midnight growth factor for a given size.

The raw DMA/APS size distributions as well as the TDMA hygroscopic growth distributions were inverted and smoothed using a version of the Twomey algorithm derived from Twomey (1965, 1975), and Markowski (1987). The Twomey-based

inversion accounts for the possibility of multiply charged particles, particle loss in the instrument, and broadening of the transfer function due to diffusion.

The RH and volatility, corrected with the midnight calibration scans, were inspected to determine the dominant soluble inorganic species present in the ambient aerosol. The individual distributions from each RH scan were first inverted and smoothed using the method described in the previous paragraph. Upon completing the inversion each distribution was fitted using a combination of lognormal distributions, and example distribution is shown in figure 5. The data for each analyzed RH scan was compiled allowing easy quantitative analysis to determine the dominant inorganic species present for each specific scan. Deliquescence relative humidities (DRH) of interest in this region are 40% corresponding to ammonium bisulfate and 80% corresponding to ammonium sulfate (Martin, 2000). A similar approach for each volatility scan was taken to create a volatility/temperature series plot. Similarly, volatility temperatures for both ammonium bisulfate and ammonium sulfate, both near 200ºC, allow sulfates to be distinguished from other aerosol types in the region such as organic, which volatilize at significantly higher temperatures (Jennings et al., 1994). This approach was used to further determine the soluble and insoluble aerosol characteristics for the specific time series in the region. The analyzed DRH and crystallization RH (CRH) were used to constrain the aerosol composition.

The inverted size and size-resolved hygroscopicity distributions will be used along with the dominate aerosol type, determined from deliquescence, crystallization,

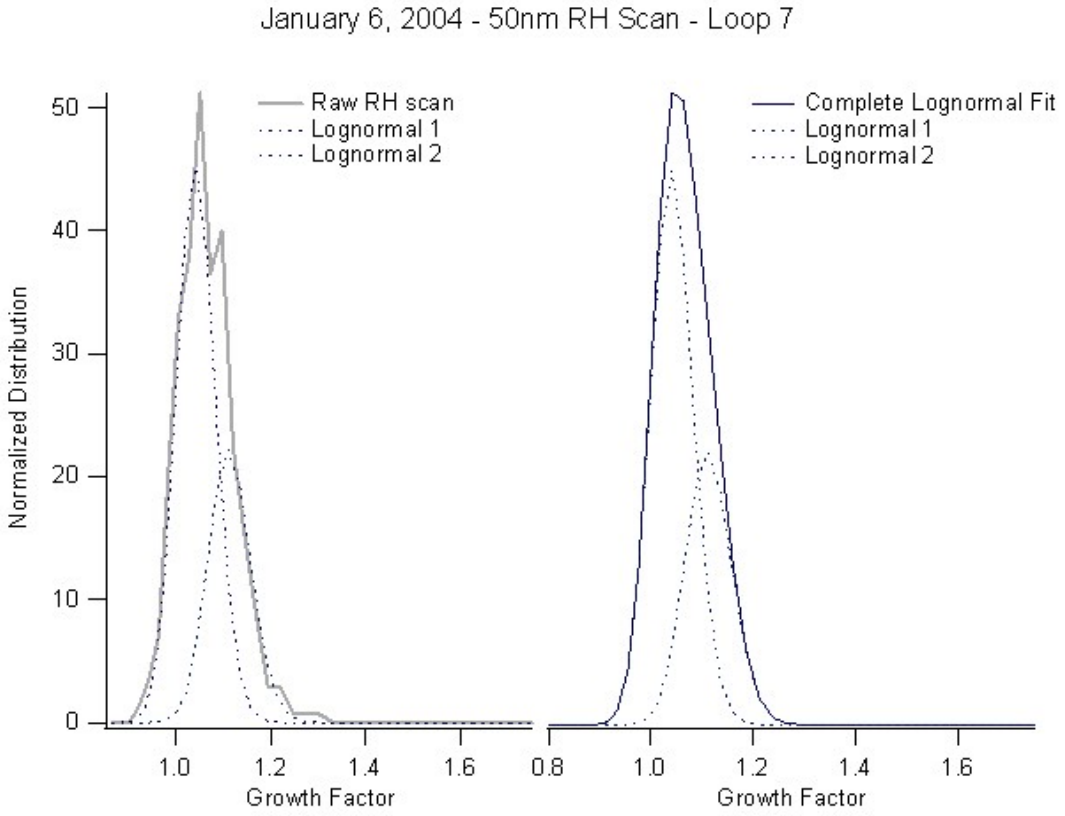

Fig. 5. Comparison showing a raw RH loop and corresponding lognormal fitting.

and volatility scans, to calculate the size distributions for both the soluble and insoluble portions. The insoluble fraction of the sub micron size distribution was assumed to be composed of a mixture of organic carbon (OC) and elemental carbon (EC) based upon data obtained at the IMPROVE site located in the park. The ratio of OC to EC was calculated using data measured at the IMPROVE sampling site within the park and found a OC/EC ratio of 9 to 1. The supermicron mode in this region is dominated by dust, either from local or remote sources. Biomass burning in South America can episodically have an impact on the coarse mode, however results from the BRAVO study indicate that the mass concentration attributed to biomass burning is dwarfed by dust a majority of the time (Kuhns et. al., 2005). Assumptions made concerning the dominant inorganic species were also made by utilizing data analyzed from each RH and volatility scan. To calculate the soil and coarse mass (CM) terms of the Reconstruction Equation, soil was assumed to be the fraction of the coarse mode less than 2.5μm, while CM was considered to be the fraction greater than 2.5μm. The soluble fraction was computed using a method where the density and activity for a specific solution is determined using empirical fits provided by Tang and Munkelwitz (1994; Tang et al., 1997). The soluble and insoluble mass size distributions were created for each scan using the assumptions described above. Each soluble and insoluble mass size distribution was fitted with a series of up to two lognormals for both the fine mode and the coarse mode. Figure 6 shows the comparison of the lognormal best fitting and the soluble mass distribution for several distributions from December 2003.

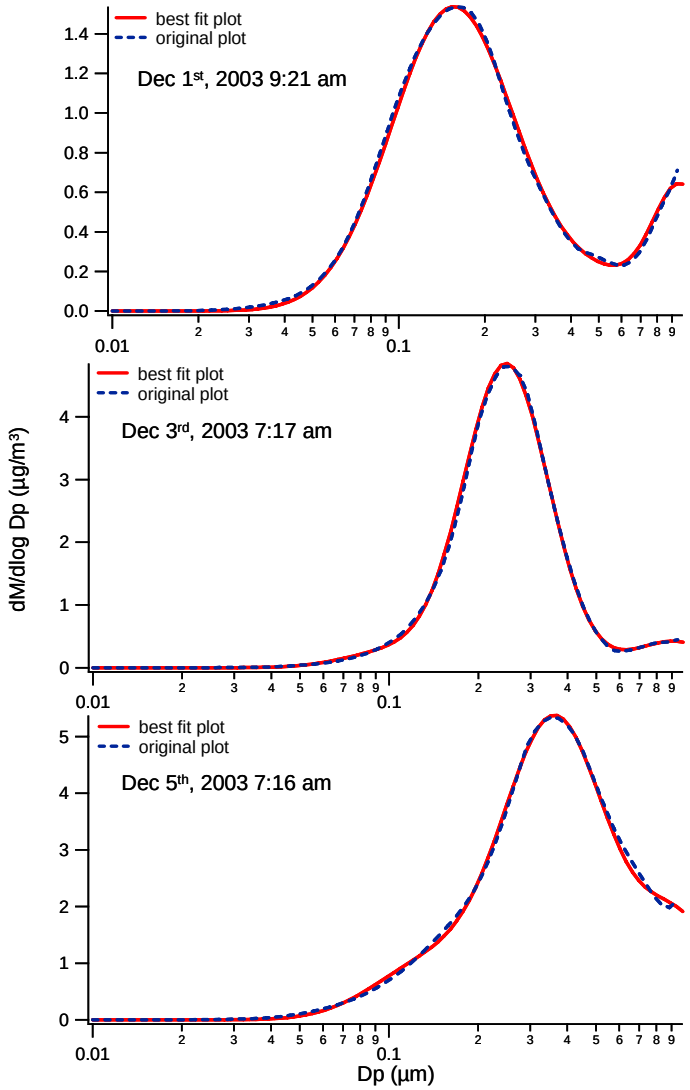

Fig. 6. Comparison of the lognormal best fitting and the soluble mass distributions for several distributions from December 2003.

The mixing state of the aerosol can have a significant impact on the mass extinction efficiencies for particle species considered in the Reconstruction Equation. However, it can be quite difficult to determine whether the aerosol particles are internally or externally mixed. An internal mixture is when aerosol particles of a given size contain an identical mixture of compounds from each source. Conversely an external aerosol mixture is one were the aerosols present have distinctly different compositions. Many research groups focus entirely on externally mixed aerosols due to the complexity in calculating internally mixed aerosol mass extinction efficiencies. Focusing strictly on externally or internally mixed aerosols can lead to significant errors if the incorrect mixing state is chosen. To reduce errors in the mass extinction efficiencies both internally and externally mixed aerosols were considered.

To calculate the externally mixed mass extinction efficiencies, the median diameter, standard deviation, refractive index, and density for each particle species, based on lognormal mass size distribution fits, were used with Mie theory to calculate the extinction and corresponding mass size distribution for each separate species. Each extinction and mass size distribution for all aerosol species considered were then integrated to compute the total species specific extinction coefficient $\left(b_{ext,i}\right)$ and species specific total mass concentration $\left(m_{D,i}\right)$. The externally mixed extinction efficiencies were then calculated using the following equation.

$$\alpha_i = \frac{b_{ext,i}}{m_{D,i}} \tag{5}$$

Calculating the internally mixed mass extinction efficiencies is far more complex than determining externally mixed mass extinction efficiencies. The relationship governing the total extinction for an aerosol comprised of sulfate, OC, and LAC is given by the following:

$$b_{ext} = \alpha_{SO4} m_{SO4} + \alpha_{OC} m_{OC} + \alpha_{LAC} m_{LAC} \quad (6)$$

Since it is not feasible to isolate the contributions to the final extinction coefficient for the internally mixed aerosol, a modified approach was used. The approach taken here was to individually increase then decrease each individual particle types concentration separately. The ratio of the change in the total extinction coefficient to the change in the mass concentration for each particle class perturbed will then be calculated. This may not be identical to the actual mass extinction efficiency, and thus will be referred to as the mass extinction sensitivity, α' and is described by the following:

$$\alpha' = \frac{\Delta b_{ext,i}}{\Delta m_i} \quad (7)$$

Using the mass extinction sensitivities for each particle type in Equation 1 will not necessarily produce the correct extinction coefficient. It was assumed for this study that the ratio of the mass extinction efficiencies is equal to the ratio of the mass extinction sensitivities.

The *f(RH)* was calculated for both sulfate and nitrate by utilize the size distribution lognormal fits for both internally and externally mixed aerosols. The size distributions composed partially or entirely of sulfate or nitrate were theoretically altered to the measured ambient RH measured at the IMPROVE sampling site within the park,

or the climatological average used by the IMPROVE network. The *f(RH)* is calculated by:

$$f(RH)_i = \frac{b_{ext(RH)_i}}{b_{ext(dry)_i}} \tag{8}$$

$b_{ext(RH)}$ is the extinction calculated at the modified RH and $b_{ext(dry)}$ is the extinction calculated at low RH. Extinction was calculated using the methods described for the internal and external mass extinction efficiencies. The refractive index and density will be calculated using empirical relationships for the density, activity, and refractive index of a solution as a function of mass fraction of water using a process described earlier by Tang and Munkelwitz (1994). Uncertainty in the distribution of particles between the upper and lower leg of the hysteresis loop results in uncertainty in the calculated extinction coefficient. It can however be quite difficult to establish on which leg of the hysteresis loop the aerosol resides. Ascertaining on which leg the aerosol lies requires an RH history to which the aerosol has been exposed. Using an extensive network of surface observations can help in ascertaining an RH history. However in west Texas surface observations are spatially sparse and often interrupted. To minimize error in assuming what leg of the hysteresis loop the aerosol lies, a separate approach was used were all the calculated *f(RH)* values for each season were fitted with a two-parameter fit devised by Koontz et al. (2003) of the form:

$$f(RH) = a\left(1 - \frac{RH}{100}\right)^{-b} \tag{9}$$

CHAPTER IV

ANALYSIS OF DATA

The data presented in the following discussions will be presented chronologically from Spring (April 2003) to Winter (January 2004). During the four separate sampling periods 549 size distributions and corresponding hygroscopic growth factor distributions were measured at the IMPROVE sampling site. Through the spring, 178 size distribution were measured, 48 in the summer, 185 in the fall, and 138 in the winter. During the summer sampling period, the initial failure of the air conditioning system in the trailer and a lightning strike causing components to fail was responsible for the small number of size distributions recorded. The size distributions measured during spring and summer were combined with APS size distributions. During the fall and winter, however, the APS was unavailable due to scheduling conflicts, limiting size distributions to the submicron size range.

Before inspecting more detailed aspects of various parameters, the fundamental properties of the aerosol in Big Bend should be recognized. While size distributions in the Big Bend area can fluctuate appreciably with time, the seasonal average of all size distributions sampled can be useful in attaining the average conditions for each season. The average size distributions for each season can also be utilized as a comparison, allowing particular events to easily be scrutinized as normal or irregular conditions.

Figure 7 shows the average number distribution for each season, while figure 8 shows the average volume distribution for each season. The lowest aerosol

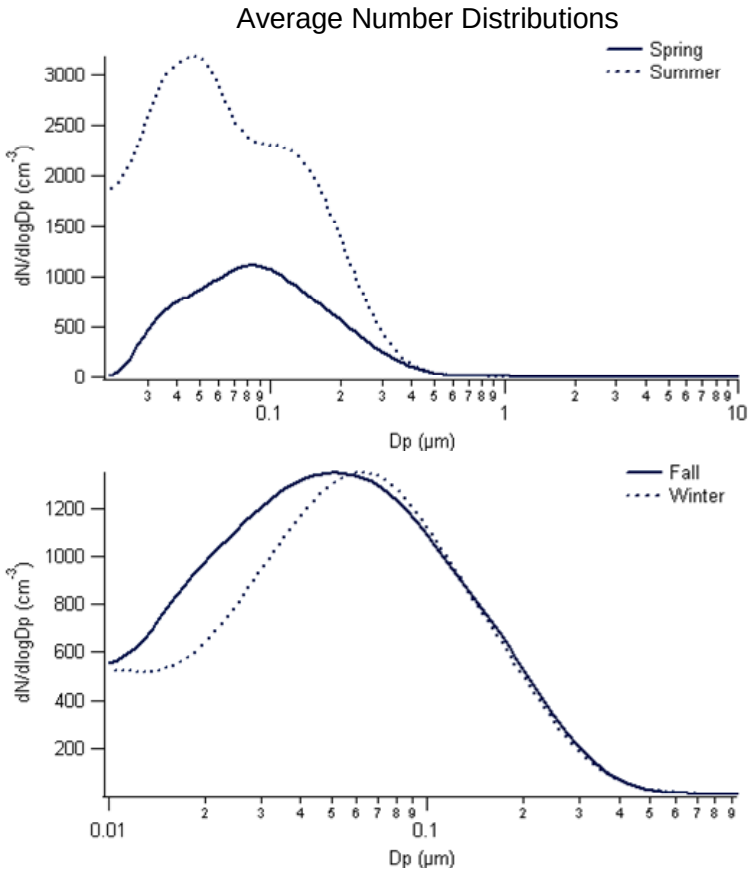

Fig. 7. Average number distributions for each season at Big Bend National Park.

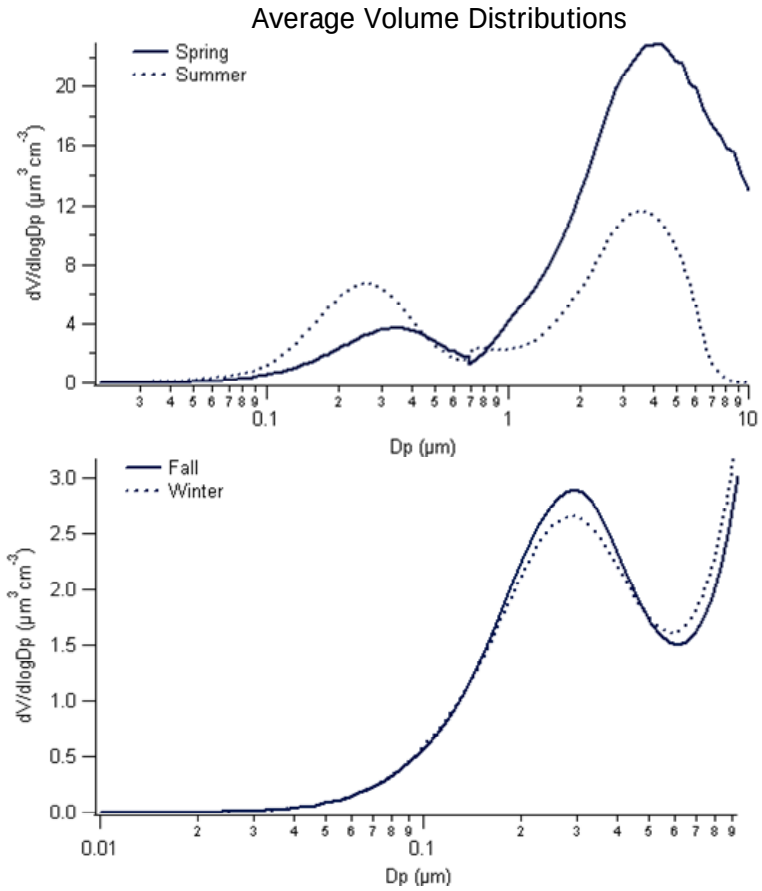

Fig. 8. Average volume distributions for each season at Big Bend National Park.

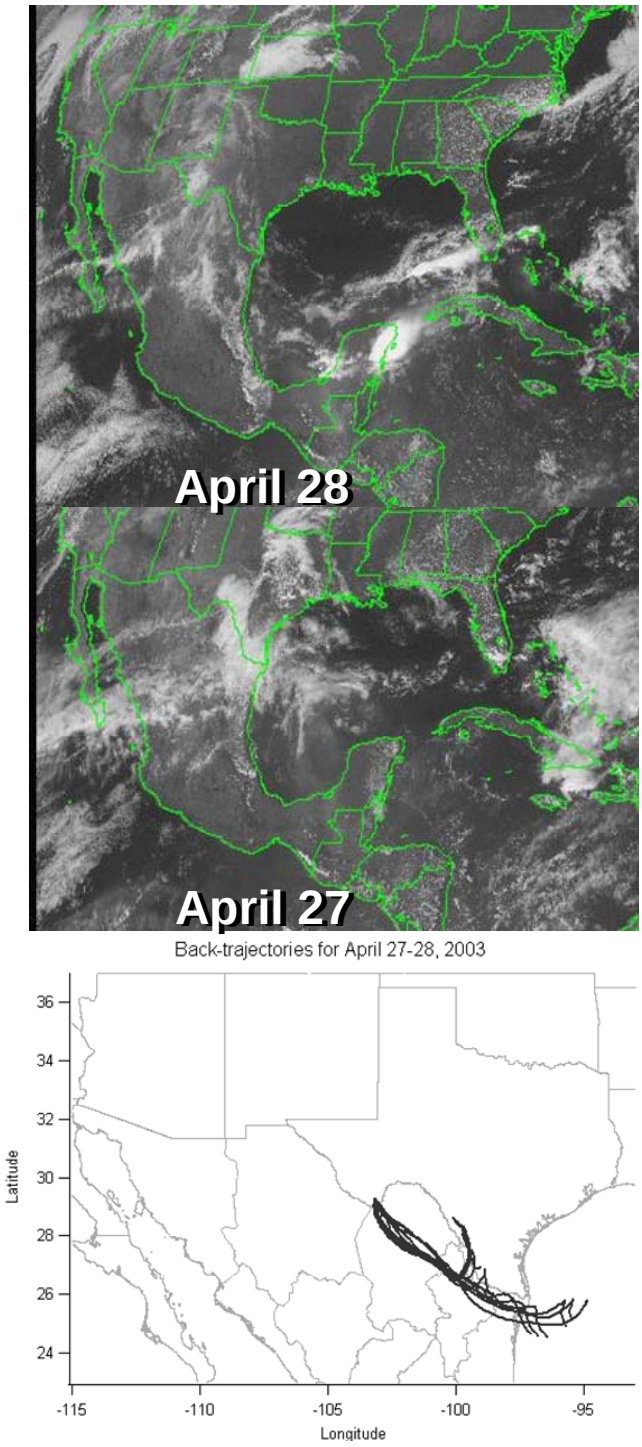

Fig. 9. April 27 and 28, 2003 satellite images, back-trajectories calculated for April 27-28, 2003.

concentration was observed during the spring, with a peak found approximately at 0.085µm. Although the lowest aerosol number concentration was observed in the spring, the highest aerosol volume concentration was measured during the season. The spring volume distribution is dominated by the supermicron mode. An increased modal diameter, located at 0.095µm, is also observed during the spring number distribution when compared to other seasons. Low aerosol concentration, increased modal diameter and minimal growth factors indicate the aerosol was influenced by biomass burning, similar to findings of Lee et al. (2005). Satellite images and back trajectories, displayed in figure 9, strengthen the assumption that the submicron aerosol concentration was most likely influenced by biomass burning in South America during the spring. Biomass burning in South America was shown to intermittently affect the accumulation mode during the 1996 scoping study (Kreidensweis et. al., 2001; Hand et. al., 2002). The summer size distribution demonstrated a significantly higher aerosol concentration than any other season. Two modes are easily distinguishable, the major mode occurs at 0.045µm while the minor mode is located near 0.055µm. The higher aerosol concentration was presumably caused by a bulk of the air mass trajectories originating from the southeast, similar to previous findings (Gebhart and Malm, 2000; Gebhart et. al., 2001; Hand et. al., 2002). Inspecting figure 8, the volume concentration in the summer is slightly lower than in the spring, and is bimodal. The summer volume distribution, unlike the spring, isn't dominated by either mode. The fall and winter size distributions are nearly identical with total aerosol concentrations falling between the spring and summer concentrations. The fall size distribution peak is easily identified at

0.055μm, while the winter is slightly higher at 0.065μm. Volume distributions for the fall and summer are virtually indistinguishable, each with a submicron peak near 0.3μm.

A time series of average aerosol size distributions observed over period of a day were constructed by combining distributions sampled during each hour of the day. These were be used to identify how mountain and valley breezes, as well as solar intensity can create diurnal aerosol size distribution cycles. The daily averaged number distribution is shown in Figure 10, while the daily averaged volume distribution is displayed in Figure 11. A quick Inspection of figure 10 emphasizes the elevated summer aerosol concentration, roughly four times that of the other three seasons. The peak located at 0.045μm dominates the number distribution during the summer. Several diurnal cycles become evident when the data is analyzed closely. During the spring, nucleation events were regularly seen at around 1600 local time (LT). A similar nucleation event can be found in the fall and winter distributions as well, at 1500 and 1700 LT, respectively. Each daily averaged number distribution, excluding the summer distribution, exhibits a mode that undergoes growth from early evening to roughly noon. Specifically, the summer mode grows from 0.02μm at 1630 LT to 0.085μm at 1100 LT. While the fall mode grows from 0.015μm at 1400 LT to 0.06μm at 0800 LT and the winter mode exhibits the most growth, growing from 0.01μm at 1630 LT to 0.08μm at 1130 LT. While the summer size distribution exhibits no mode growth, it does show evidence of a pronounced nucleation event at 1930 LT.

The spring volume distribution in figure 10 highlights the influence the supermicron mode has on the volume concentration for the season. Unlike the number

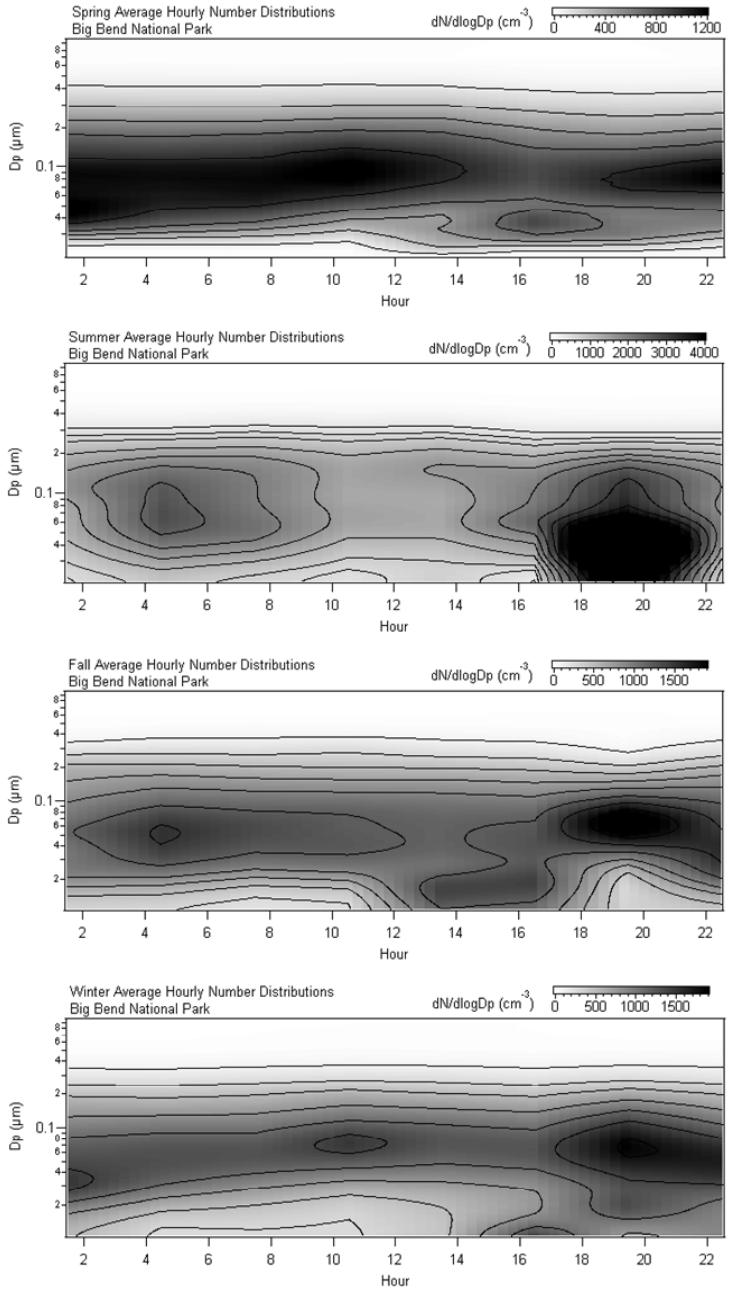

Fig. 10. Average diurnal number distributions.

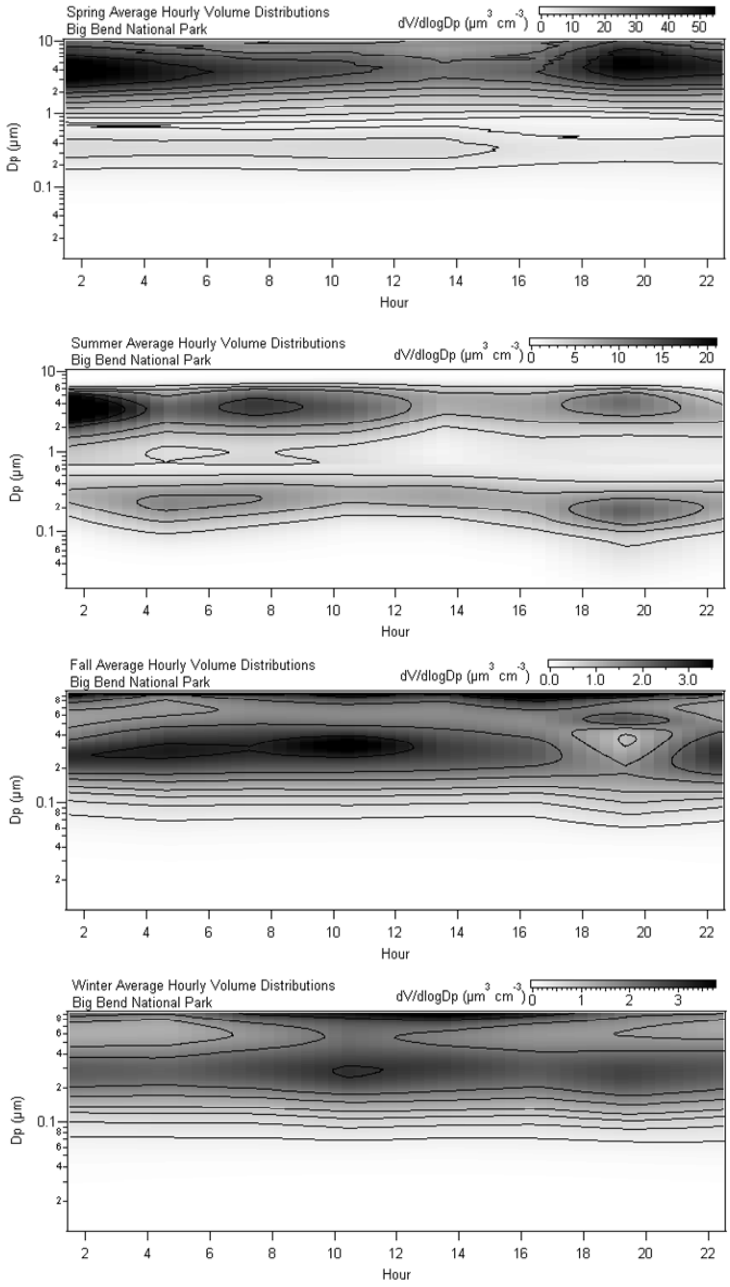

Fig. 11. Average diurnal volume distributions.

distributions that show a diurnal cycle of aerosol particle growth, the volume distribution does not appear to exhibit a mode that grows in any diurnal cycle. However, an enhancement in the supermicron mode is visible in both the spring and summer volume distributions during the evening and over night hours. Analyzing the available meteorological data from the Panther Junction ranger station showed that enhanced wind speeds from late afternoon well into the night are common in the park. The local evening mountain breezes, causing an increase in dust levels, are most likely responsible for the increase in the supermicron volume concentration. It should be noted that increased wind speeds in the late afternoon hours are common, according to the meteorological database, thus the elevated dust diurnal cycle would in all probability be present in the fall and winter distributions had the APS been available to characterize it.

The complete time series of number concentration distributions coupled with the total number concentration for spring, summer, fall, and winter is shown in figure 12. The complete time series of volume concentration distribution together with the total volume concentration for the same season listed above is shown in figure 13. Periods where the total volume and number concentration is zero are times when the instrument was not functioning properly.

During each season, the total number concentration rarely exceeded 3000 particles per cm^3. A closer look indicates that total number concentration during the spring and winter is well below that measured during the summer and fall. Throughout the summer, number concentrations were higher than during any other season, averaging roughly 2500 particles per cm^3. The diurnal growth cycle present in the daily averaged

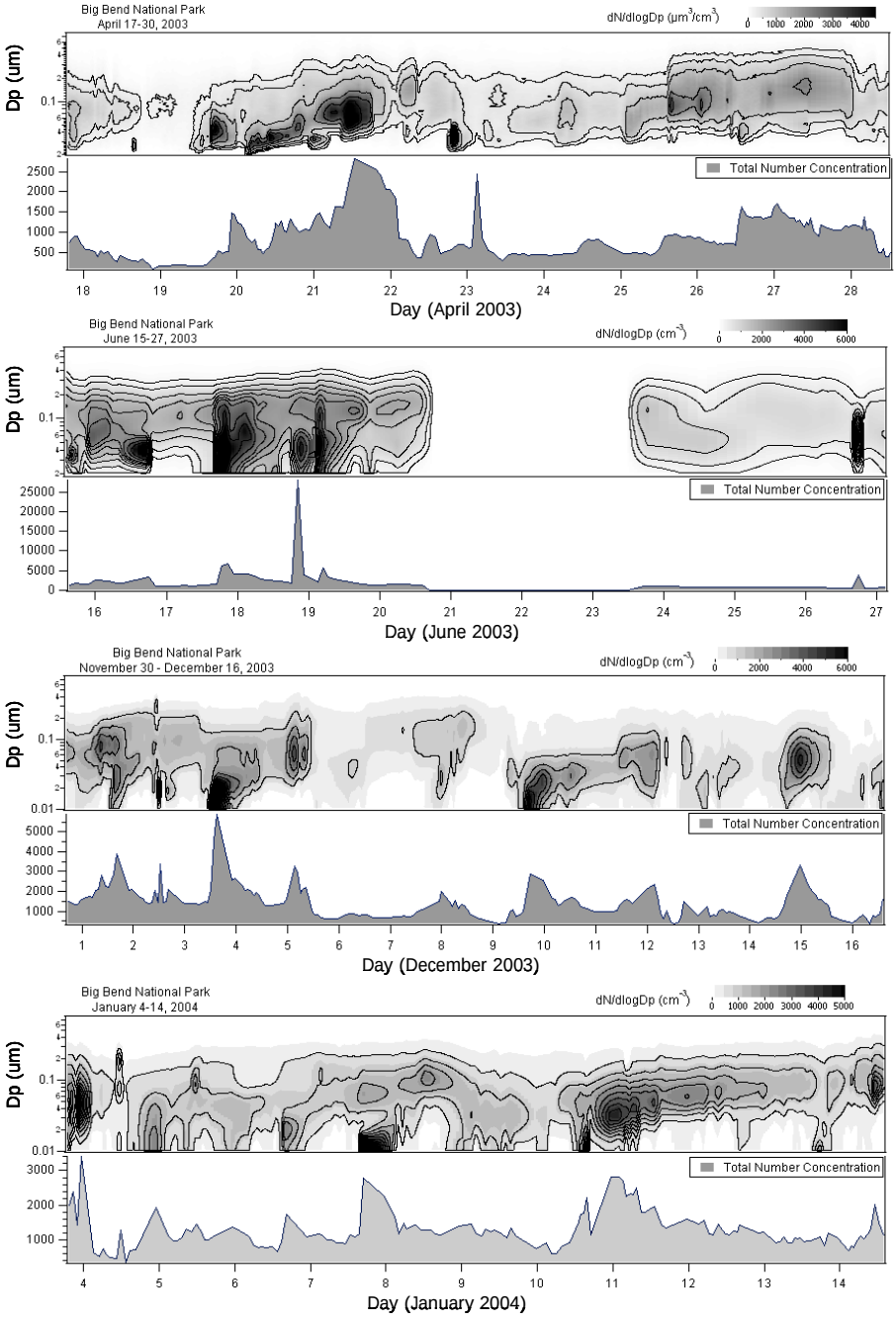

Fig. 12. Seasonal aerosol number distributions and total number concentrations.

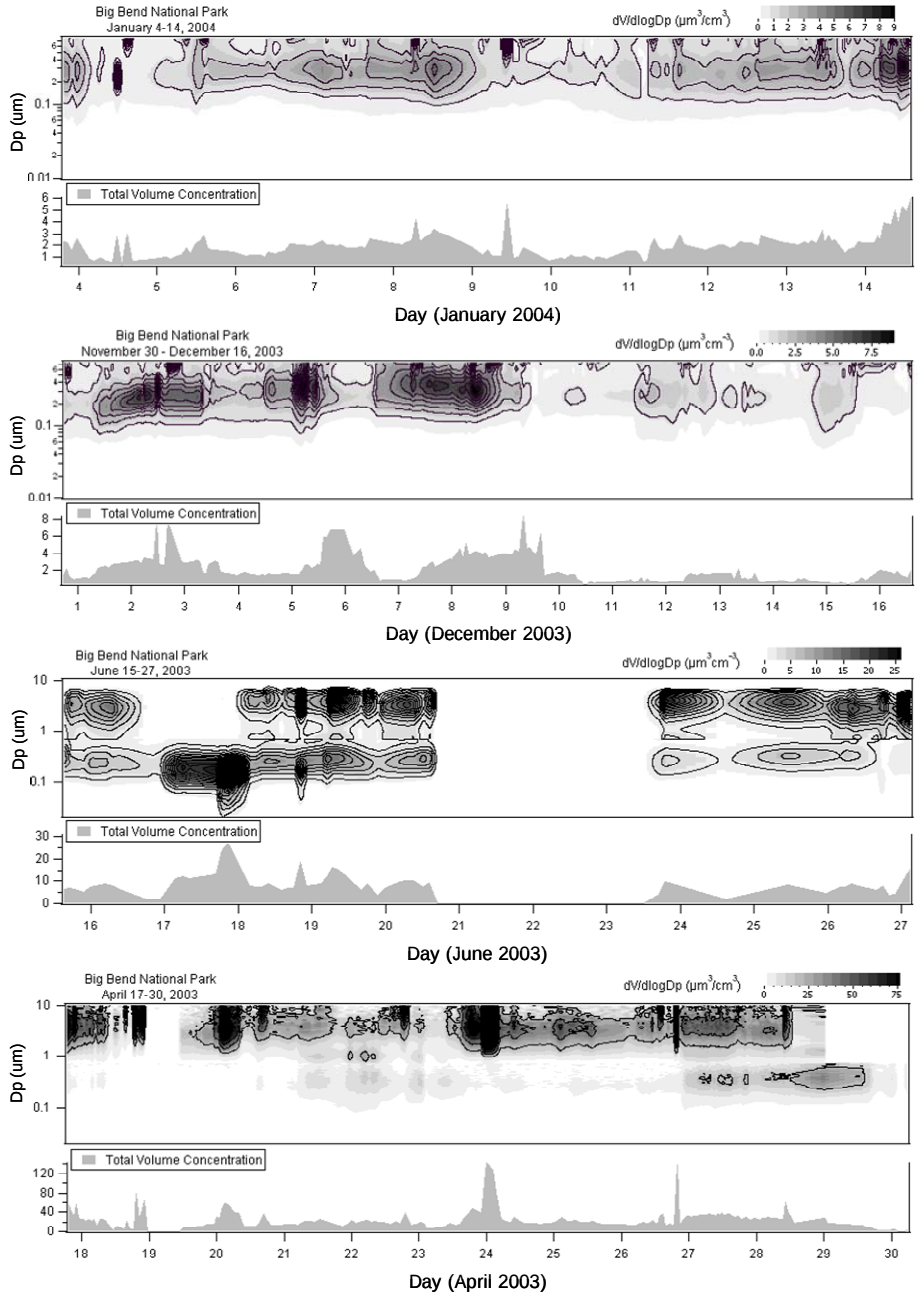

Fig. 13. Seasonal aerosol volume distributions and total volume concentrations.

number concentration, shown in figure 10, is quite clear in the spring and winter seasonal number distributions. In fact, during the winter sampling period these diurnal cycles are seen on six straight days from January 3rd to 10th. Calculated trajectories for all scans during this six day diurnal growth episode suggest air mass source regions varied from the southwest around to the north-northeast, indicating variable source regions impacting the sampling site during the diurnal growth episode. Embedded within the previous diurnal cycles are three multi-day growth events, the first is April 20th through the 22nd, the second January 6th through the 8th, and lastly January 10th through the 13th. The spring multi-day growth event began with a nucleation event near midnight on the 20th. Particle growth was most likely initially dominated by coagulation, with a decrease in number concentration and an increase in volume concentration, after a frontal passage near noon the next day, post frontal winds shifted from the North and a high pressure set in, creating an inversion layer trapping previous coagulated particles along with newly transported particles. This would explain the increased number concentration during the coagulation process. During the winter sampling phase both multi-day growth events began with a nucleation event late in the day. Particle growth for both episodes appears to be caused by coagulation. The number concentration spike associated with both aerosol nucleation events is followed by a dramatic decrease in number concentration, and a slight increase in volume concentration, consistent with particle growth by coagulation. Aerosol hygroscopicity distributions are shown in figures 14, 15, and 16 for spring, fall, and winter respectively. Summer hygroscopicity distributions are not shown. The limited data, during the

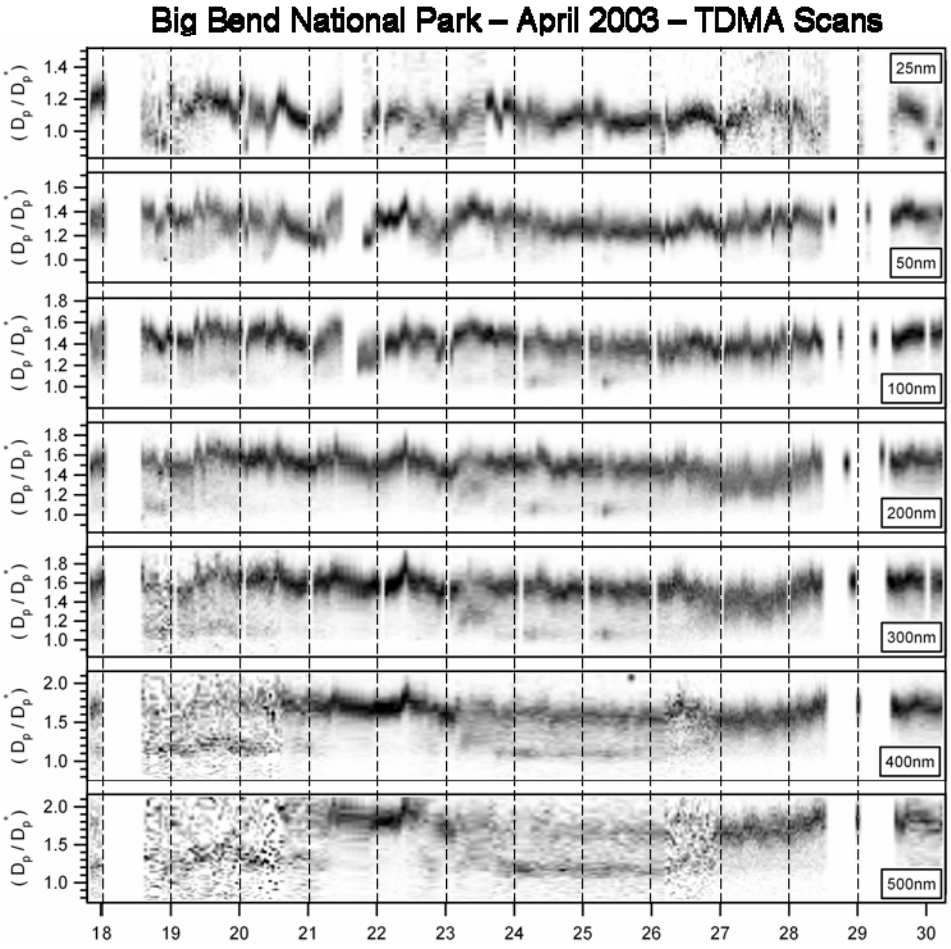

Fig. 14. April 2003 TDMA scans.

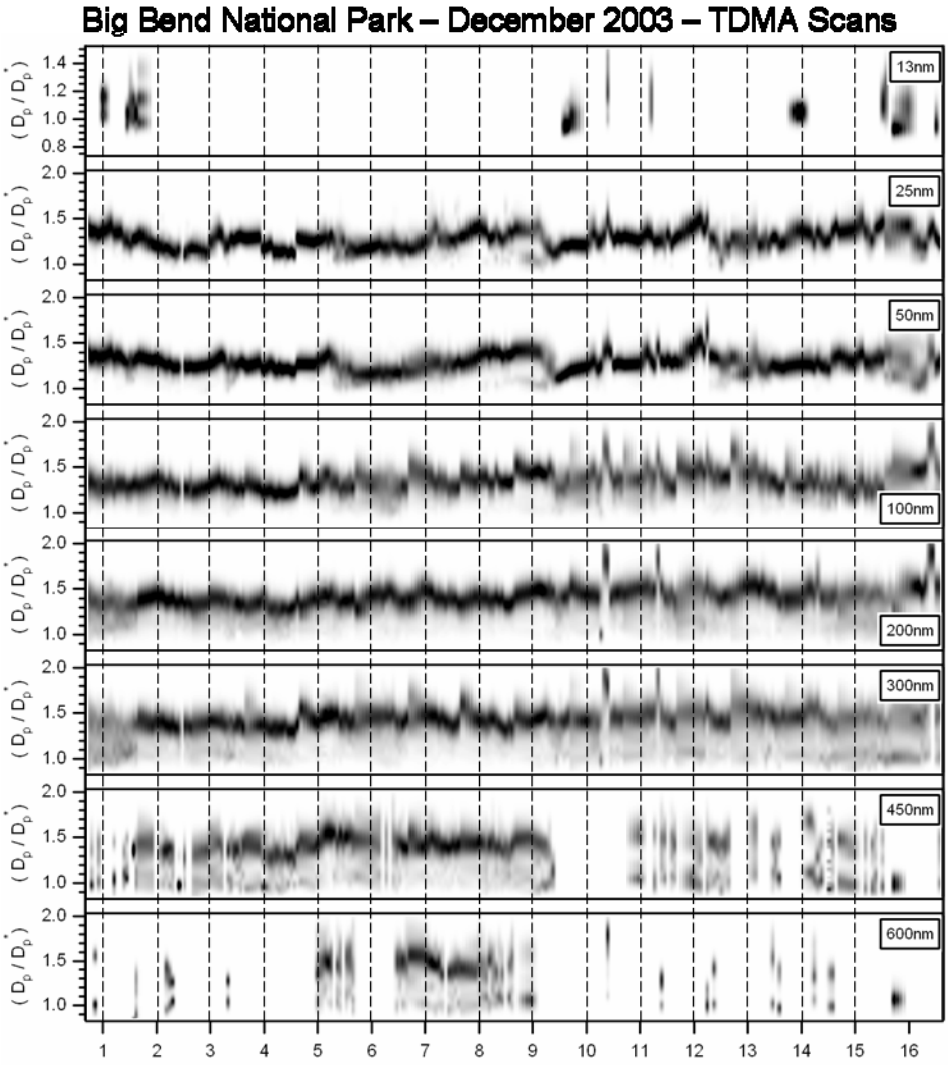

Fig. 15. December 2003 TDMA scans.

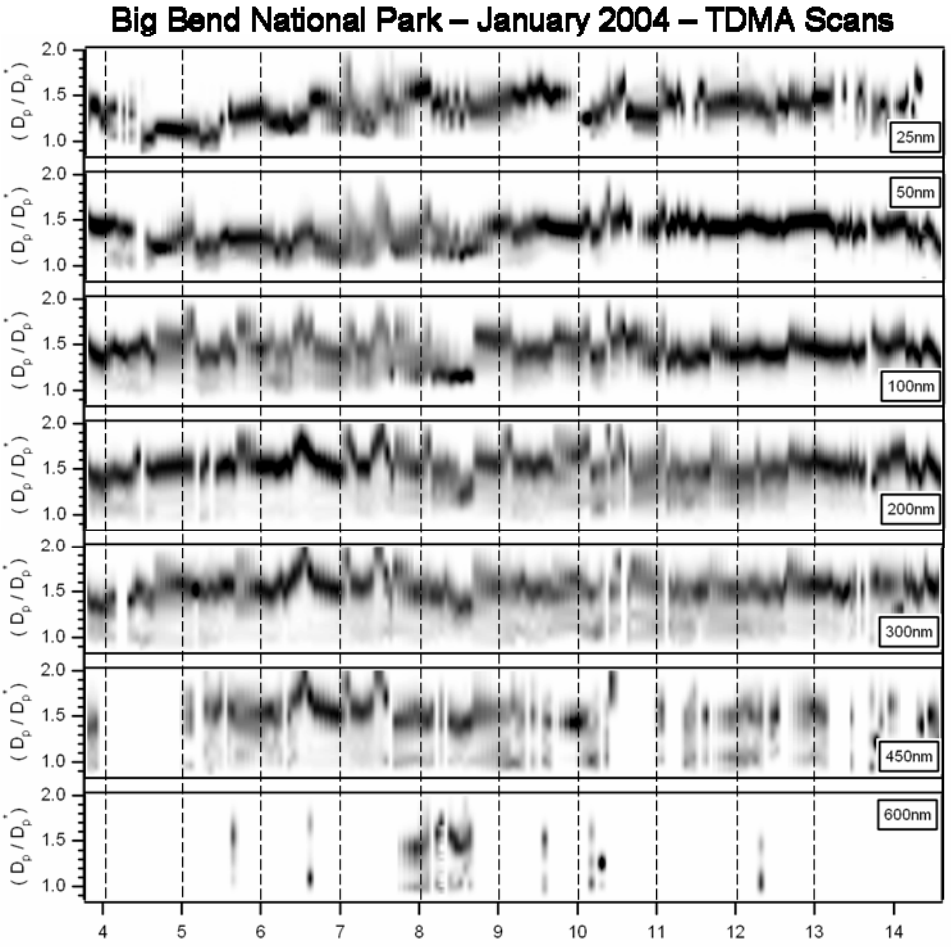

Fig. 16. January 2004 TDMA scans.

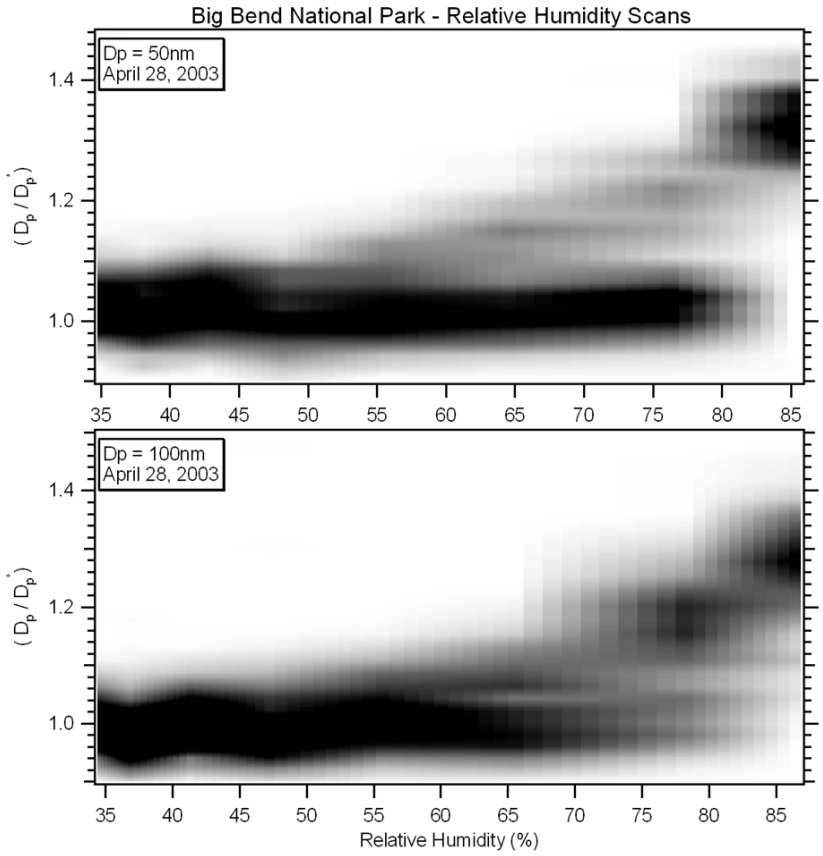

Fig. 17. Spring 0.5 and 0.1µm deliquescence scans – April 28, 2003

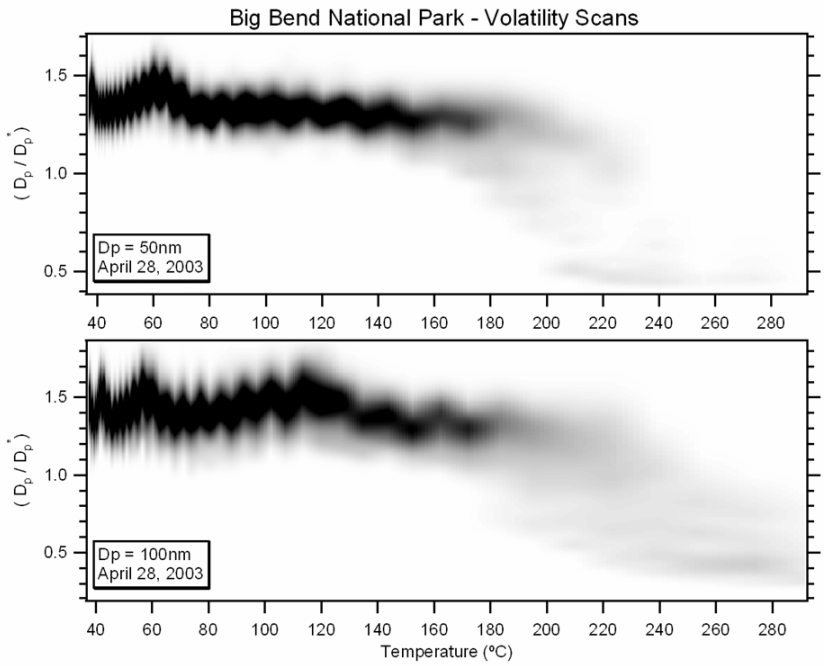

Fig. 18. Spring 0.5 and 0.1µm volatility scans – April 28, 2003

summer sampling period makes it difficult to ascertain any trends that may have been measured. The hygroscopicity distributions obtained were used to determine the soluble and insoluble components of the aerosol, particle mixing state, and the dominate soluble aerosol species present for each season. A complete RH scan is composed of both a deliquescence scan and a crystallization scan. A quick inspection of seasonal hygroscopicity distributions reveals a majority of distributions were monomodal in nature, which is consistent with an aerosol that is internally mixed, as would be expected for a remote region such as this.

Spring hygroscopic distributions indicated that 0.025µm and 0.05µm particles were quite non-hygroscopic, with 0.025µm growth factors reaching a minimum on the 25th and 26th at 1.05 and 0.05µm growth factors for the same days were found to be 1.2. However, figure 14 shows hygroscopic growth factors for the remaining particle sizes (0.1µm, 0.2µm, 0.3µm, 0,4µm, and 0.5µm) are very near those of a pure ammonium sulfate aerosol. Deliquescence scans completed on April 28th, shown in figure 17, indicate a DRH of 80% for 0.05µm particles and 76% for 0.1µm particles. Crystallization scans are not shown for the spring due to specific program issues not known at the time. Volatility scans completed directly following the previous RH scans on April 28th, shown in figure 18, indicate an aerosol that volatilizes at near 210ºC. Volatility temperatures of ammonium sulfate and ammonium bisulfate are nearly indistinguishable, volatilizing at approximately 200ºC, while other species that may be present such as ammonium nitrate, sodium chloride, and sulfuric acid, volatilize at

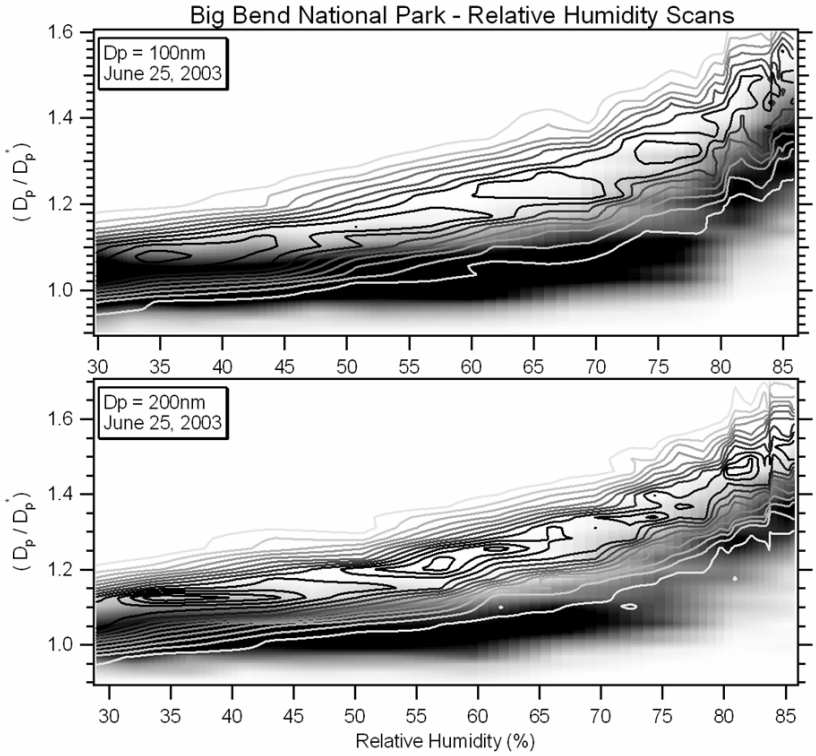

Fig. 19. Summer 0.1 and 0.2µm deliquescence and crystallization scans – June 25, 2003.

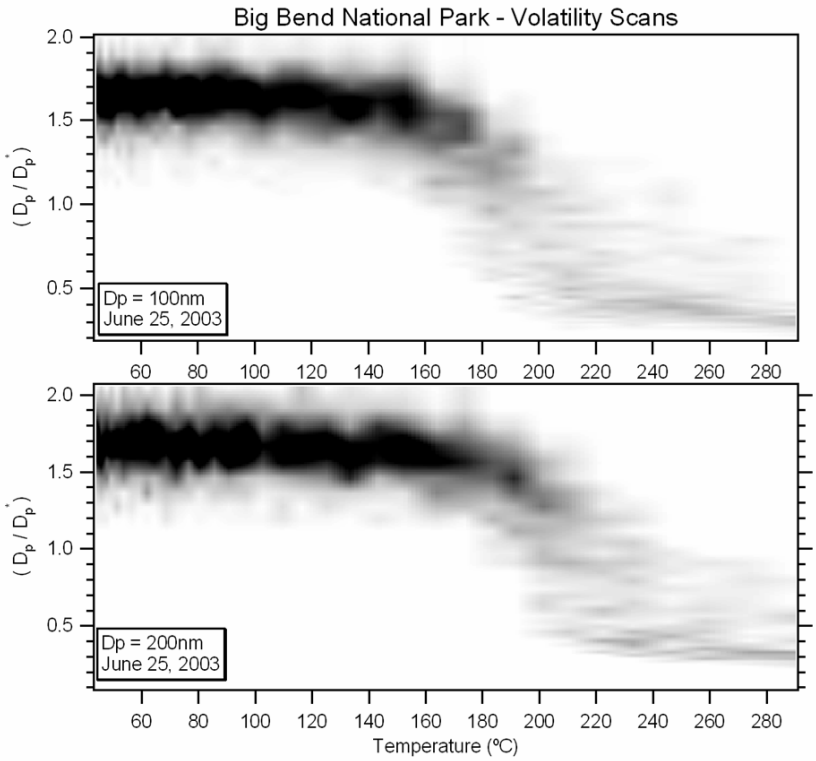

Fig. 20. Summer 0.1 and 0.2µm volatility scans – June 25, 2003.

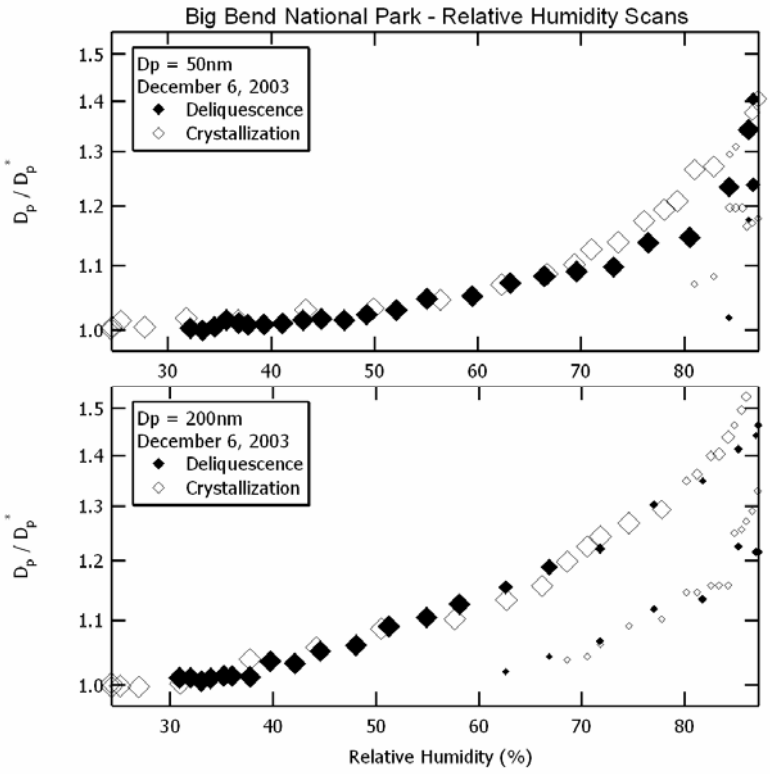

Fig. 21. Fall 0.05 and 0.2µm deliquescence and crystallization scans – December 6, 2003

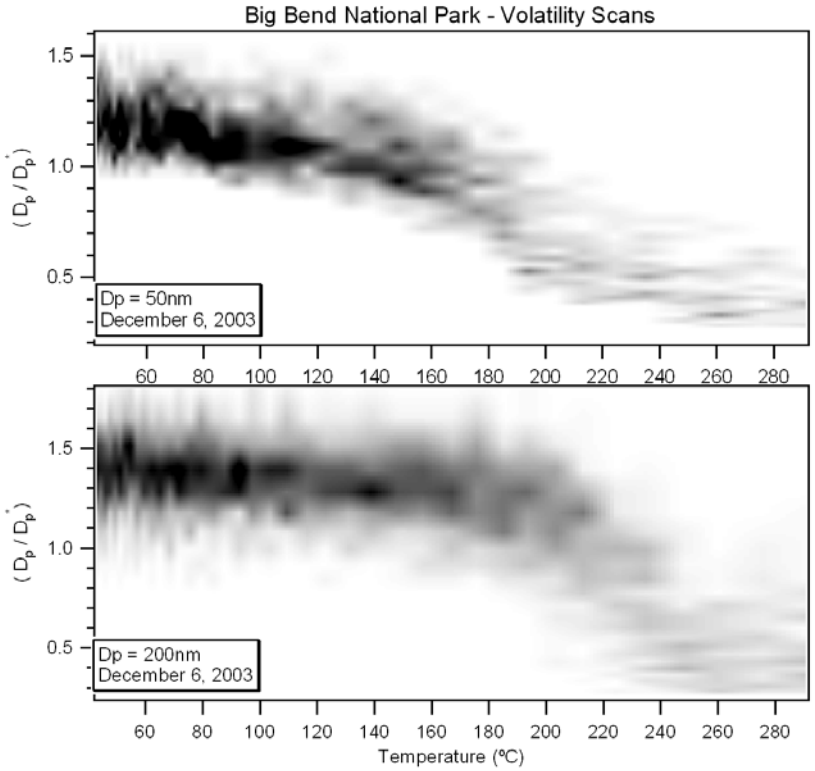

Fig. 22. Fall 0.05 and 0.2μm volatility scans – December 6, 2003.

temperatures different than that of ammonium sulfate and ammonium bisulfate (Johnson et al., 2004). The volatility scans completed during the spring sampling period support the conclusions that the primary hygroscopic compounds contained sulfate. The Deliquescence and volatility scans displayed are indicative of the majority of scans completed during this period. While the measured DRH suggest an aerosol dominated by ammonium sulfate, growth factors in both deliquescence scans fell well below that of pure ammonium sulfate, suggesting an internally mixed aerosol composed of ammonium sulfate and organics.

Summer RH scans shown in figures 19 and 20 respectively, completed on June 25th, show that 0.1µm particles had a DRH of 79%, while 0.2µm particles had a DRH of 76%. This offset in deliquescence could be due to the presence of an organic core with the sampled aerosol population. Similar to the RH scans completed during the spring, the DRH for both particle sizes signify an aerosol dominated by ammonium sulfate. Volatility temperatures of 200ºC and 210ºC were measured for 0.1µm and 0.2µm particles, respectively. The measured volatility temperatures indicate a sulfate dominated aerosol. Analogous to that observed in spring, the growth factors measured are well below those of pure ammonium sulfate. Thus, the same assumptions made during the spring can be applied to the summer sampling period.

Fall RH and volatility scans were completed each day for 0.050 and 0.2µm particle sizes. Nearly 80% of the RH scans completed during the fall were similar to those completed on December 6th, shown in figure 21. The RH scans in figure 21 do not show a DRH for either the 0.050 and 0.2µm particles. The lack of hysteresis in the

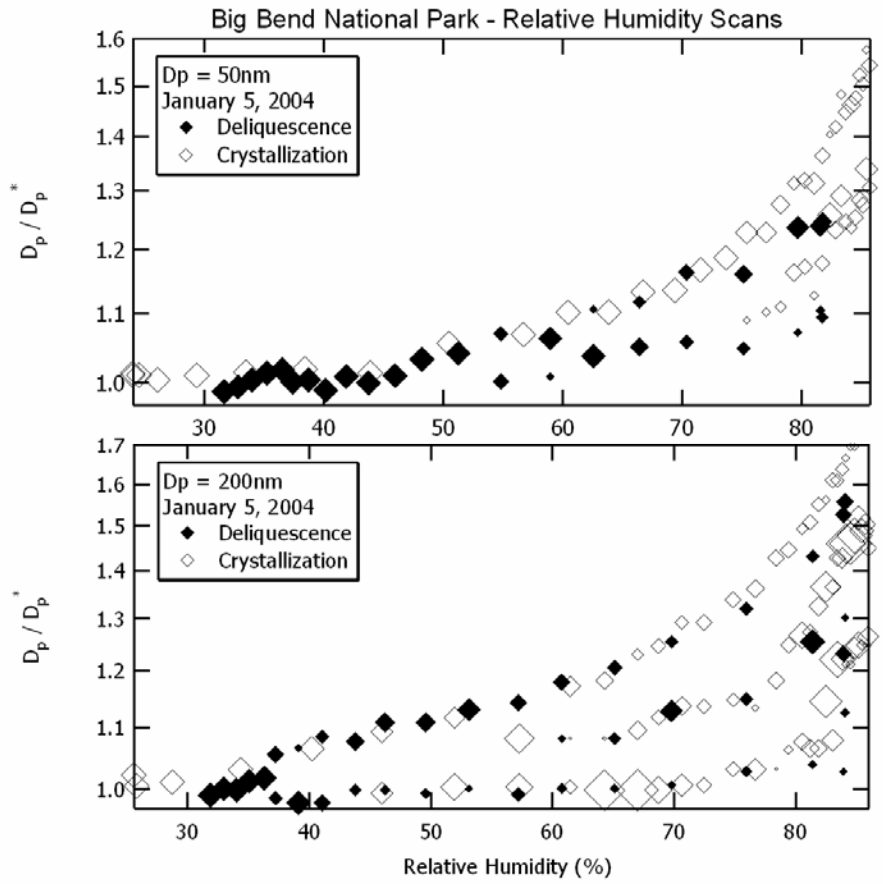

Fig. 23. Winter 0.05 and 0.2µm deliquescence and crystallization scans – January 5, 2004.

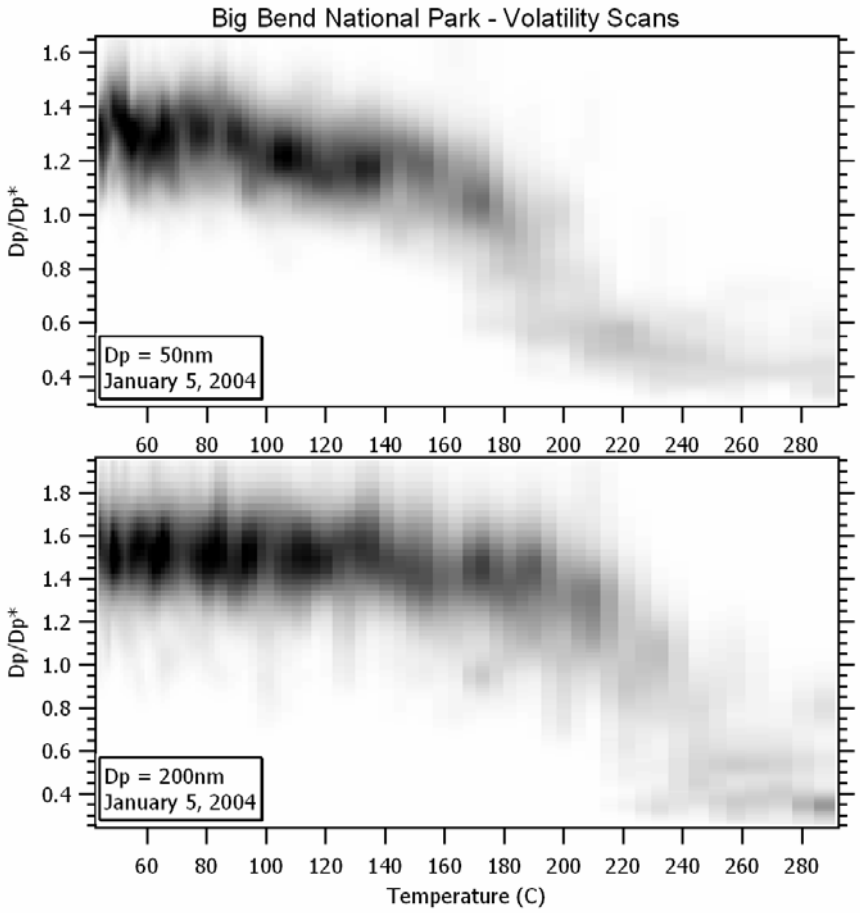

Fig. 24. Winter 0.05 and 0.2µm volatility scans – January 5, 2004.

seasonal RH scans is consistent with an ammonium bisulfate dominated aerosol. Volatility scans completed just following each RH scan indicate volatility temperatures of 195ºC and 210ºC for 0.050 and 0.2µm particles, respectively. The RH and volatility scans indicate that the dominate hygroscopic aerosol type sampled during the fall ammonium bisulfate.

RH and volatility scans were completed for 0.050 and 0.2µm particle sizes during the winter sampling period. Comparable to the fall, a vast majority of the RH and volatility scans for the winter phase were similar in appearance. The RH scans shown in figure 23 were completed on January 5th and, analogous to the fall, no clear DRH can be determined from the data. Again, the lack of hysteresis in the RH scans during the winter indicates an aerosol dominated by ammonium bisulfate. The volatility scans shown in figure 24, which were completed just following each RH scan indicate a volatility temperature of 190ºC and 215ºC for 0.050 and 0.2µm, respectively. The winter volatility scans, similar to that observed during the previous season, indicate sulfate dominated inorganic aerosol type. The volatility and RH scans indicate that the dominate inorganic aerosol for the season was presumably ammonium bisulfate.

The aerosol size distributions and hygroscopic data were used along with the established dominate hygroscopic aerosol to calculate the soluble and insoluble mass concentration distributions and multiple extinction distributions for each scan completed during all four seasons. The steps for calculating aerosol extinction along with soluble and insoluble mass are described in the Analysis Methods section. Aerosol extinction was calculated for a dry environment, 80% RH environment, RH measured at the

IMPROVE site, and NPS seasonal average RH. Figure 25 shows the seasonal dry extinction distributions and corresponding total dry extinction. The spring and summer volume distributions are dominated by dust in the supermicron mode; however each of the extinction distributions is dominated by the submicron mode. This is largely due to the enhanced extinction efficiencies of submicron particles with diameters greater than 0.1μm over particles found in the supermicron mode. While each season had a peak total extinction of roughly 60 Mm^{-1}, average seasonal extinctions varied. Average aerosol extinction (b_{ext}) peaked during the summer, consistent with that described in the historical database (Gebhart et. al., 2001) at nearly 25 Mm^{-1}, and dipped to near 11 Mm^{-1} in the winter, again consistent with the historical database. While the average aerosol extinction trend follows what other studies have found for the Big Bend region, the average aerosol extinction values are significantly lower than what previous studies have found (Gebhart et. al., 2001; Malm et. al., 2003). This presumably could be due to the increased convection within the region from summer 2003 to early 2004. During the period of June 19th to June 28th, stations within the park measured the annual average rainfall, most likely causing increased wet deposition within the region.

The mass extinction efficiencies described extensively in the Analysis Methods section were calculated using two different methods. The calculated mass extinction efficiencies for each season are shown in Table 1. It is not surprising that the calculated mass extinction efficiencies for this study deviate from those the EPA sets forth as for use in the Reconstruction Equation, since these defaults are used for every location

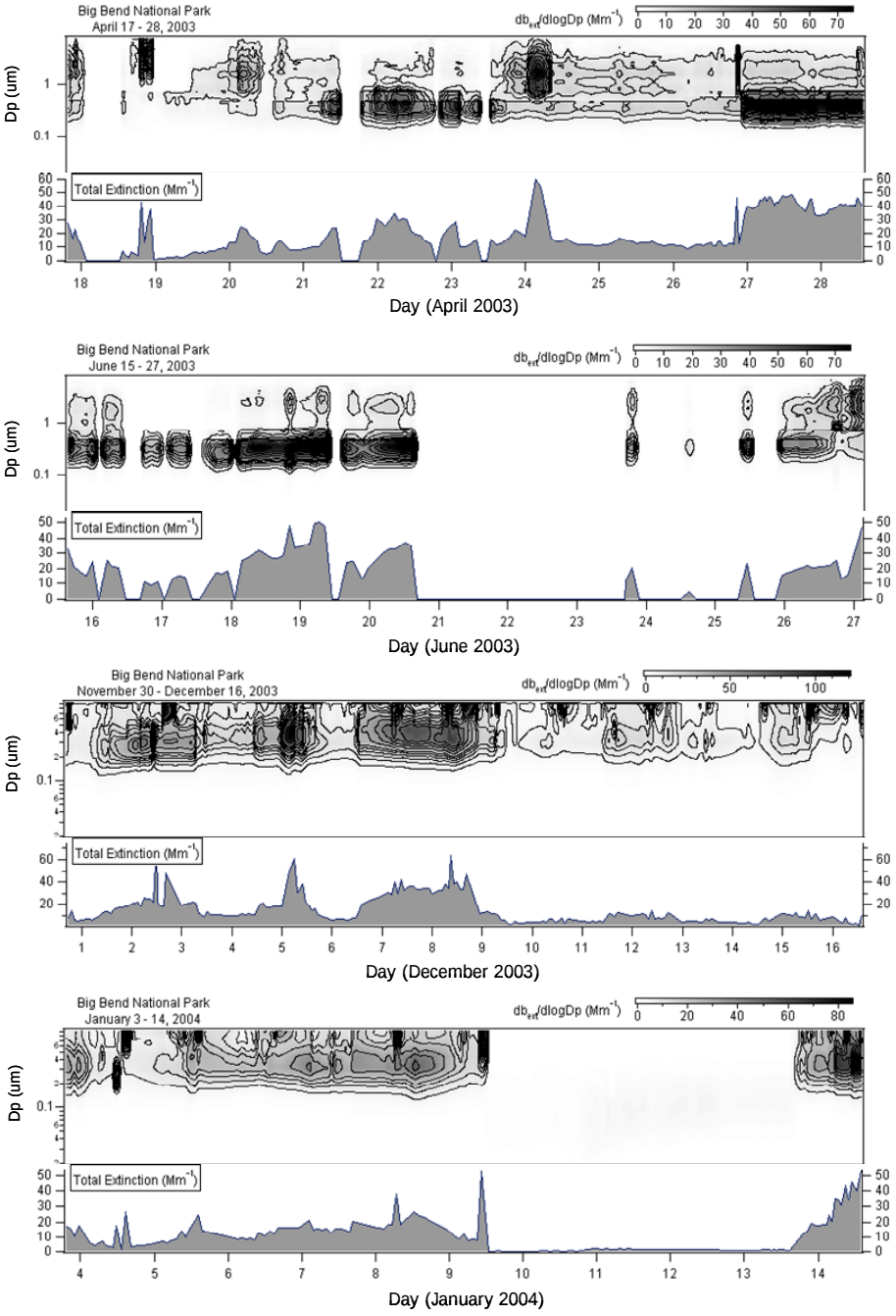

Fig. 25. Seasonal aerosol extinction distributions, and total extinction.

Table 1. EPA and calculated mass extinction efficiencies (m^2/g) and *f(RH)* for each sampling season conducted in Big Bend National. EM – external mixture, IM – internal mixture.

	Spring		**Summer**		**Fall**		**Winter**		**Average**
	EPA	This Study	EPA	This Study	EPA	This Study	EPA	This Study	
α_{soil}	1	1.023	1	0.870	1	N/A	1	N/A	**0.95**
α_{CM}	0.6	0.376	0.6	0.381	0.6	N/A	0.6	N/A	**0.38**
$(\alpha_{SO4})_{EM}$	3	3.290	3	2.675	3	2.297	3	2.346	**2.65**
$(\alpha_{SO4})_{IM}$		3.559		3.194		2.964		2.874	**3.15**
$(\alpha_{OC})_{EM}$	4	3.987	4	3.917	4	3.919	4	3.937	**3.94**
$(\alpha_{OC})_{IM}$		3.570		3.285		3.536		3.439	**3.46**
$(\alpha_{LAC})_{EM}$	10	6.995	10	7.262	10	6.921	10	6.733	**6.98**
$(\alpha_{LAC})_{IM}$		10.406		9.673		10.363		9.939	**10.10**
$(\alpha_{NO3})_{EM}$	3	3.603	3	2.963	3	3.130	3	3.173	**3.22**
$(\alpha_{NO3})_{IM}$		3.840		3.460		3.703		3.631	**3.66**
$(f(RH)_{SO4})_{EM}$	1.41	1.193	1.47	1.236	1.74	1.492	1.79	1.619	**1.39**
$(f(RH)_{SO4})_{IM}$		1.161		1.192		1.371		1.412	**1.28**
$(f(RH)_{NO3})_{EM}$		1.226		1.295		1.255		1.398	**1.29**
$(f(RH)_{NO3})_{IM}$		1.133		1.141		1.161		1.153	**1.08**
$(f(RH)_{OC})_{EM}$	1	1.024	1	1.041	1	1.035	1	1.035	**1.03**

throughout the United States and are not location specific. The soil and CM mass extinction efficiencies were not calculated for the fall and winter sampling periods due the unavailability of the APS used during the spring and summer periods. The calculated mass extinction efficiencies for soil, internally mixed sulfate and LAC are similar to the EPA default values, while coarse mass and internally mixed OC are consistently below the EPA default values. Sulfate shows a significant bias with respect to mixing state and assumed inorganic aerosol type.

The impact of the choice of the dominate hygroscopic aerosol type is evident in the values of the sulfate and nitrate mass extinction efficiencies. It should be noted that the soluble lognormal fits, described previously, were utilized to calculate both sulfate and nitrate mass extinction efficiencies. During the spring and summer periods the dominate hygroscopic aerosol type was determined to be ammonium sulfate, while ammonium bisulfate was determined to dominate the hygroscopic aerosol population during the fall and winter. The sulfate mass extinction efficiency was highest during the spring then declined with each successive sampling period. Analogous to sulfate, the nitrate mass extinction efficiency was at a maximum during the spring and declined for the summer sampling phase. However, unlike the sulfate mass extinction efficiency, the nitrate mass extinction efficiency increases for both the fall and winter to near the efficiency calculated during the spring. It is plausible to assume the decrease in the mass extinction efficiency from spring to summer was caused by a shift in the soluble number distribution, with number distribution being the only relevant variable between the two sampling periods. However, the reduction identified in the sulfate mass extinction

efficiency during the fall and winter and also the increase in the equivalent nitrate mass extinction efficiencies, is believed to be caused by the assumption made concerning the dominate inorganic aerosol between the spring and summer and the fall and winter. This assumption would have no effect on the calculated nitrate efficiency, with the nitrate refractive indices not changing with season. However, the refractive index and mass extinction efficiency of ammonium sulfate, utilized during spring and summer, differs from the properties of ammonium bisulfate, utilized during fall and winter. It is reasonable to assume that the variation in the scattering properties between ammonium sulfate and ammonium bisulfate could be responsible for the 30% reduction in sulfate mass extinction efficiencies during the fall and winter sampling periods.

Assumed particle mixing state can have a considerable effect on calculated mass extinction efficiencies. Sulfate and nitrate exhibited a slightly stronger dependence on mixing state than OC, with the difference for all three ranging from 10% to 15%. The assumption concerning particle mixing state had a more significant impact on LAC mass extinction efficiencies. Internally mixed LAC average mass extinction efficiency was 10.1 m^2/g very near the EPA default, which is 10 m^2/g, while externally mixed LAC average mass extinction efficiency was 6.98 m^2/g. While both assumed mixing state and assumed dominate aerosol type can affect mass extinction efficiencies, it appears that particle mixing state has a more significant influence. As stated earlier, the dominance of monomodal hygroscopic growth distributions in each season implies the regional aerosol approached an internal mixture. This signifies that the internal mixture mass extinction efficiencies are more appropriate for this region.

Back-trajectories of air parcels arriving 20 m above ground level at the IMPROVE site in Big Bend were calculated using the NOAA HYSPLIT4 model (Draxler, 1988) to determine whether particle mass extinction efficiencies exhibit a spatial dependency. In order to establish trajectory profiles, each trajectory was grouped depending on trajectory of arrival. This grouping method produced four distinct backtrajectory sets that are displayed in figures 26 and 27. Mass extinction efficiencies grouped by source region are shown in Table 2. Trajectories originating from the east-southeast showed increased mass extinction efficiencies, with the exception of that of LAC. Internally mixed sulfate with nitrate and OC exhibited a spatial dependence, with increased values when trajectories arrived from the southeast and northeast regions. It should be noted that the northeast region of Mexico into Texas have an increased number of anthropogenic sources. Southwest and northwest trajectories in general displayed the lowest mass extinction efficiencies, with the exception of LAC. Unlike the southeast and northeast regions, the southwest and northwest have fewer anthropogenic sources.

The calculated relative humidity extinction enhancement factor (*f(RH)*) described in the Analysis Methods section are listed in Table 1 for both externally and internally mixed aerosols. The calculated *f(RH)* values are highly dependent upon the assumed aerosol mixing state. Calculated externally mixed sulfate and nitrate *f(RH)* showed variability when compared to internally mixed. The calculated *f(RH)* values are consistently lower than the monthly averages used by the IMPROVE network. Assumptions made concerning the dominant hygroscopic aerosol had a significant effect

Table 2. Averaged source region specific mass extinction efficiencies (m^2/g).

	Northeast	**East-Southeast**	**Southwest**	**Northwest**
$(\alpha_{SO4})_{IM}$	3.369	3.736	3.220	3.204
$(\alpha_{SO4})_{EM}$	2.881	3.253	2.855	2.703
$(\alpha_{NO3})_{IM}$	3.636	4.005	3.457	3.442
$(\alpha_{NO3})_{EM}$	3.183	3.572	3.073	2.980
$(\alpha_{LAC})_{IM}$	10.127	10.228	10.137	10.073
$(\alpha_{LAC})_{EM}$	7.083	6.822	6.900	6.971
$(\alpha_{OC})_{IM}$	3.455	3.689	3.492	3.283
$(\alpha_{OC})_{EM}$	3.961	4.125	3.876	3.622

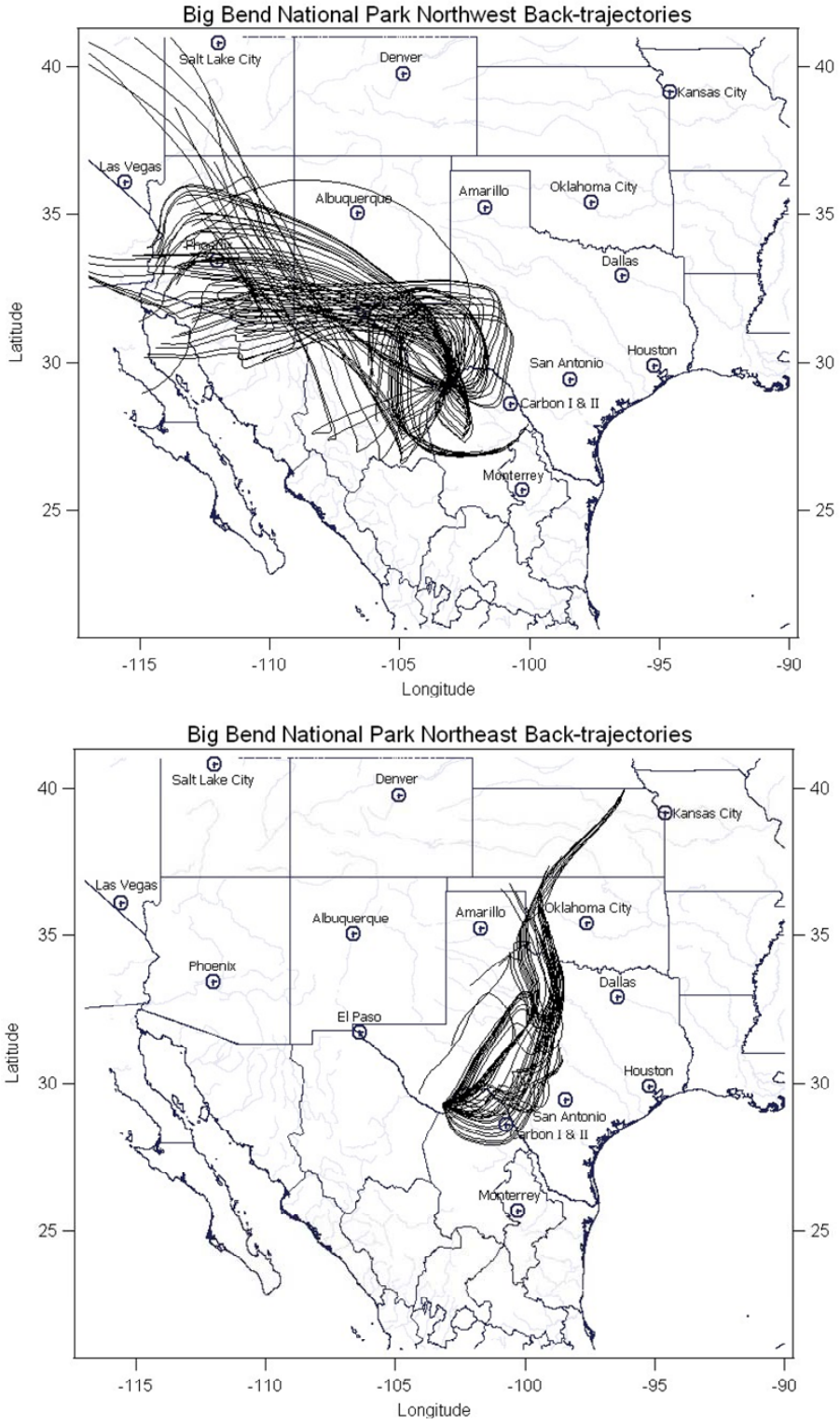

Fig. 26. Plot of Northwest and Northeast Back-trajectories.

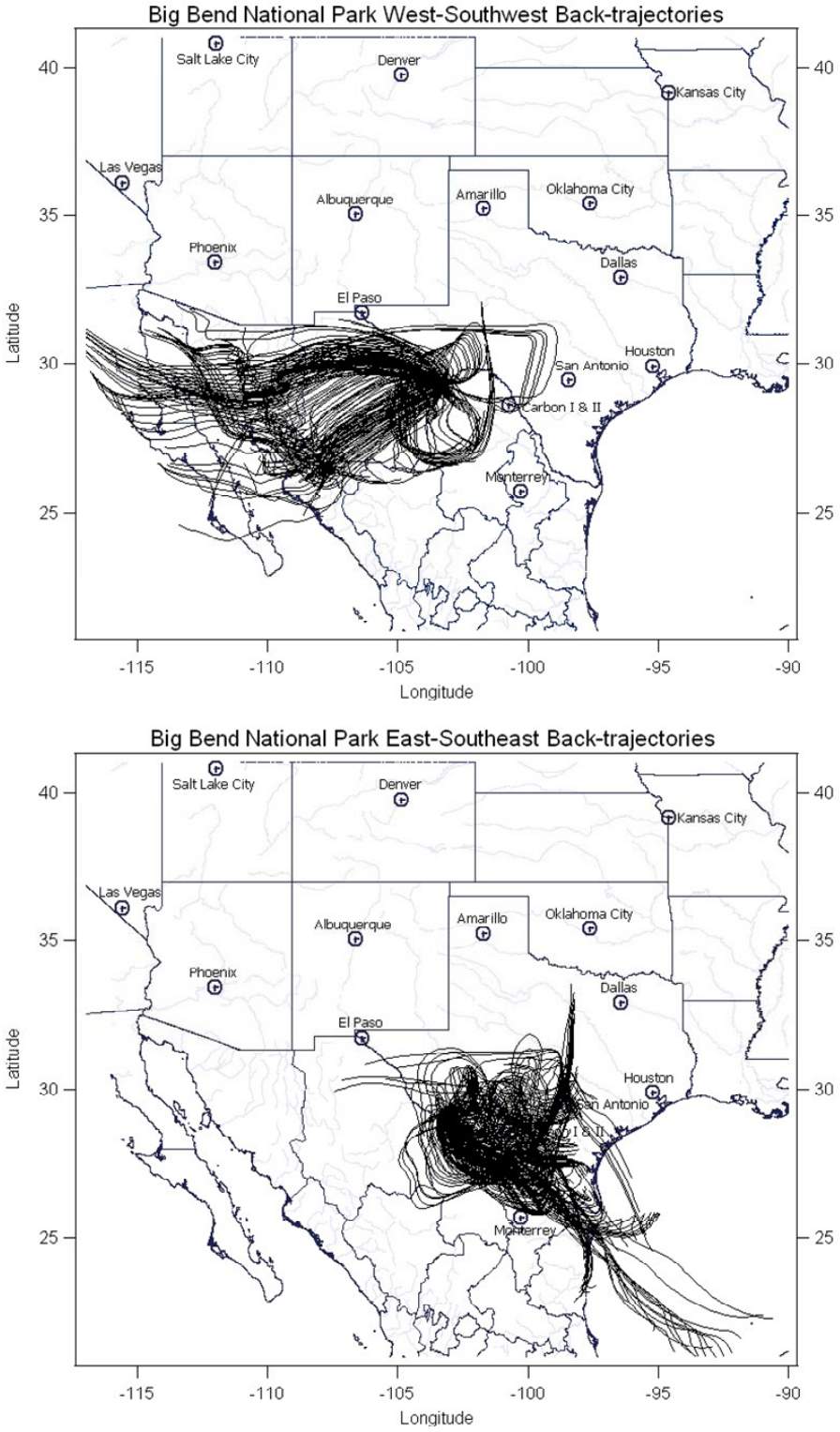

Fig. 27. Plot of West-Southwest and East-Southeast Back-trajectories.

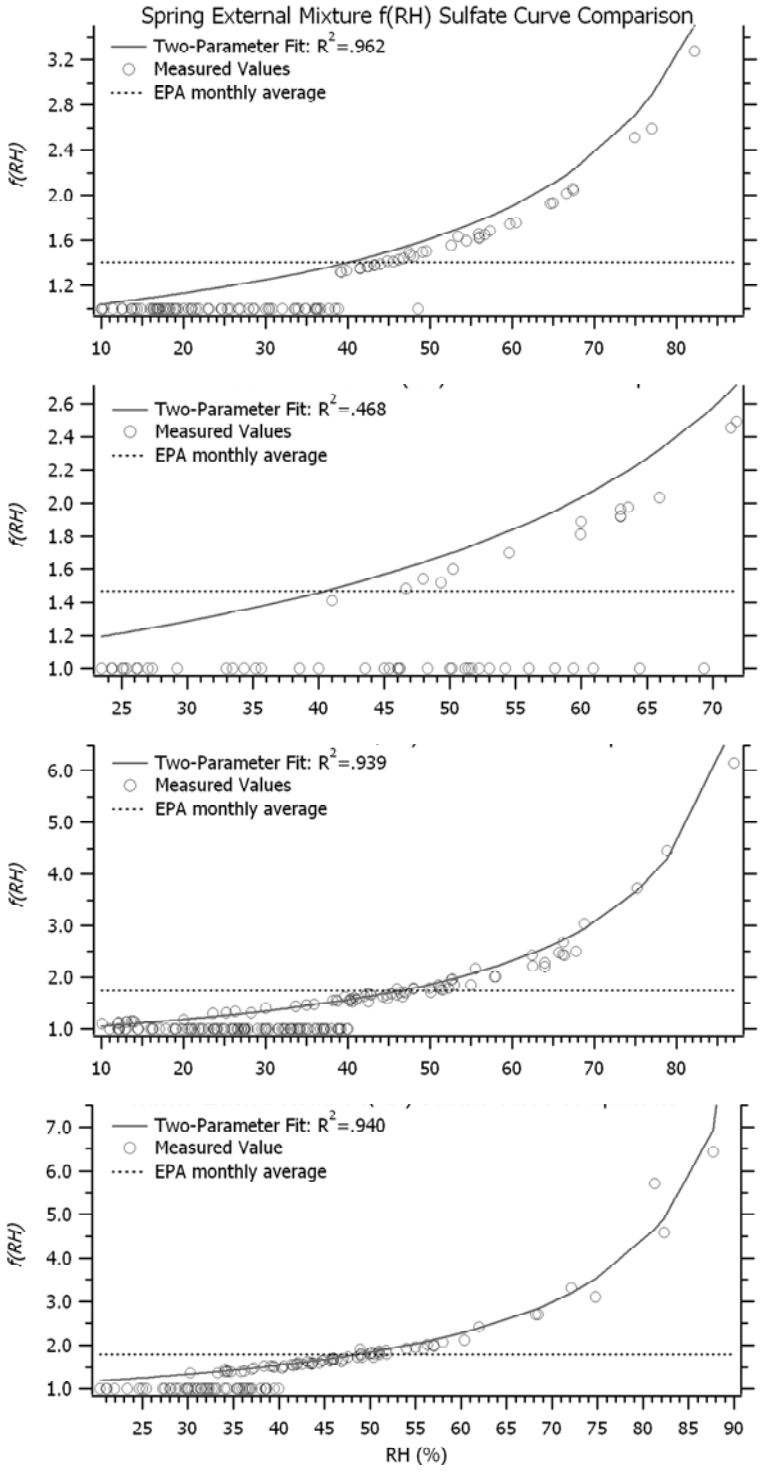

Fig. 28. f(RH) comparison plots considering an externally mixed sulfate aerosol for each season.

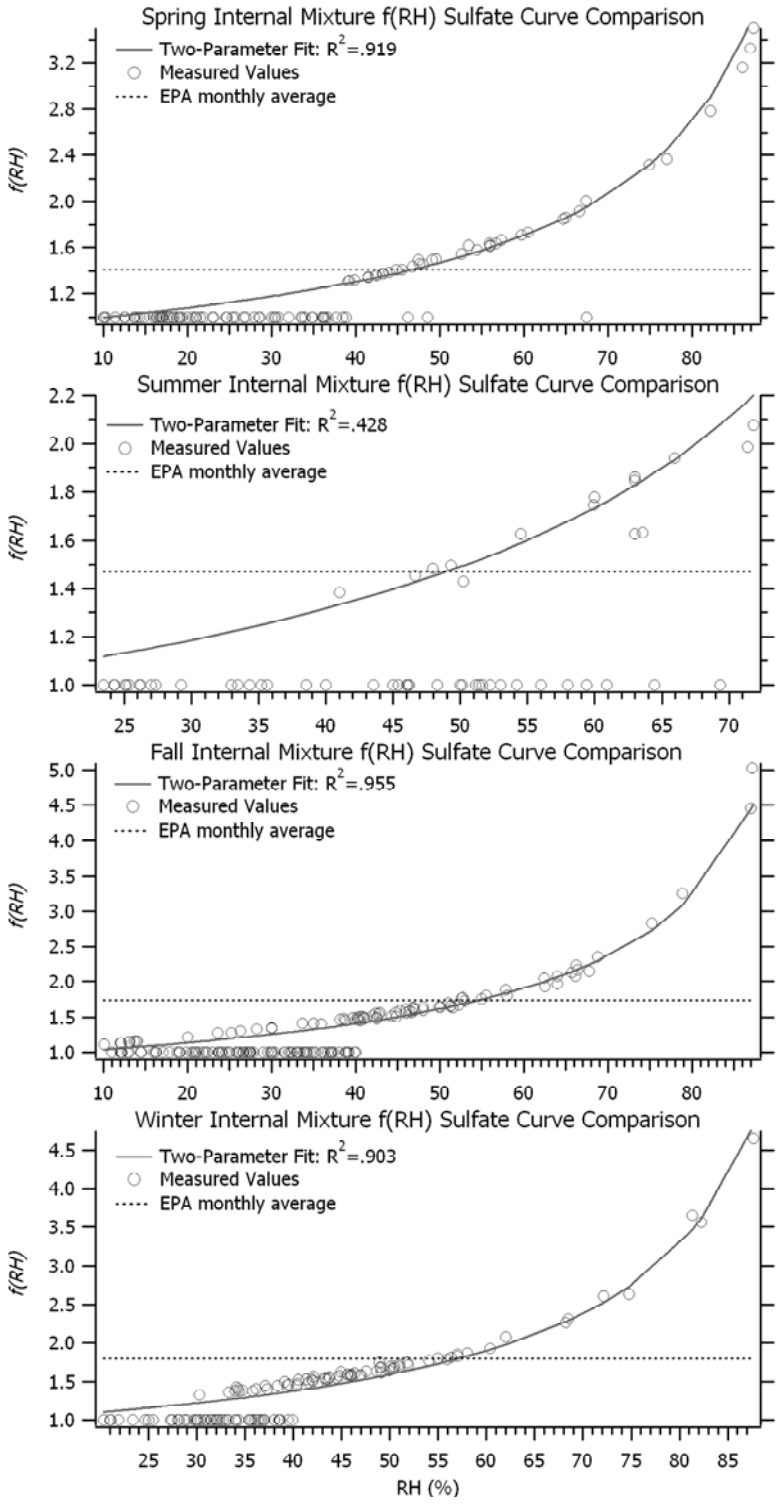

Fig. 29. *f(RH)* comparison plots considering an internally mixed sulfate aerosol for each season.

Table 3. Calculated coefficients applicable for the two-parameter fit developed by Koontz et al. (2003).

Mixing state		**Seasonal Coefficients**			
		Spring	Summer	Fall	Winter
External	a	0.96	0.96	0.95	0.95
	b	0.75	0.82	0.97	0.95
Internal	a	0.93	0.93	0.96	0.92
	b	0.66	0.68	0.75	0.79

Table 4. Averaged seasonal *f(RH)* for measured *f(RH)*, two-parameter fit *f(RH)*, and IMPROVE monthly averaged *f(RH).*

***f(RH)* Curve Comparison**			
	Measured *f(RH)*	**Two-Par Fit *f(RH)***	**IMPROVE *f(RH)***
	Internally Mixed Aerosol		
Spring	1.16	1.21	1.41
Summer	1.19	1.48	1.47
Fall	1.37	1.47	1.74
Winter	1.41	1.48	1.79
	Externally Mixed Aerosol		
Spring	1.19	1.31	1.41
Summer	1.24	1.70	1.47
Fall	1.50	1.55	1.74
Winter	1.51	1.69	1.79

on the *f(RH)* in the fall and winter months, with elevated values calculated for both seasons. The two-parameter fit formulated by Koontz et al. (2003) mentioned earlier in the Analysis Methods section allows for a more accurate *f(RH)* calculation when details regarding on which leg of the hysteresis loop the aerosol lies are unavailable. The calculated coefficients for both external and internal mixing states in each season are listed in Table 3. Only sulfate is considered for the two-parameter fit because the calculated *f(RH)* coefficients for both sulfate and nitrate differ slightly and nitrate contributes little to the overall aerosol mass in the region. Again, as one would expect, there is a discrepancy between the values calculated for each of the assumed aerosol mixing states. Shown in figures 27 and 28 are comparisons between the measured *f(RH)*, two-parameter fit calculated *f(RH)*, and the seasonal averaged *f(RH)* used by the IMPROVE network. Table 4 shows the comparison between the averaged seasonal values for the measured *f(RH)*, the two-parameter fit *f(RH)*, and the IMPROVE monthly averaged *f(RH)*. It becomes very clear that the two-parameter fit f(RH) more accurately predicts the *f(RH)* over the entire month than the IMPROVE monthly average. This is because the two-parameter fit allows for the *f(RH)* to vary dependent on the RH measured at the site. The only exception is the summer, when convection in the region was enhanced and measurements were limited, this kept the *f(RH)* values abnormally high for the season and thus the fit was higher than the IMPROVE average. Since the aerosol in the region displayed internal mixing state properties, the internal mixing state coefficients are a more accurate fit for this region.

CHAPTER V

SUMMARY AND CONCLUSIONS

Aerosol size distributions, hygroscopic growth distributions, deliquescence and crystallization properties, and volatility properties were collected using a TDMA system coupled with an APS. These data were used to calculate the seasonal and particle specific mass extinction efficiencies for the region. The data collected indicated that the submicron aerosol population was dominated by sulfate for each sampling period. Calculated aerosol extinction distributions show that the total extinction during each season was primarily dominated the submicron aerosol population, peaking during the spring and summer sampling periods. The mass extinction efficiencies calculated differed somewhat from the default values used by the EPA in the Reconstruction Equation. Each particle type's specific mass extinction efficiency exhibited a strong variability with season, with exception of OC. Mass extinction efficiencies exhibited a strong dependence upon assumed mixing state. Additionally the mass extinction efficiency of sulfate had increased variability due to assumed dominate aerosol type; ammonium sulfate for spring and summer, and ammonium bisulfate for fall and winter. Mass extinction efficiencies also showed a definite spatial dependence, when air masses originated from the southeast mass extinction efficiencies were elevated, corresponding to areas of increased anthropogenic sources. However, when air masses originated from the southwest and northwest, calculated mass extinction efficiencies where lowest, corresponding to areas of decreased anthropogenic sources.

REFERENCES

Brown, S.G., Herckes, P., Ashbaugh, L., Hannigan, M.P., Kreidenweis, S.M., Collett, J.L., 2002. Characterization of organic aerosol in Big Bend National Park, Texas. Atmospheric Environment 36, 5807-5818.

Day, D.E., Malm, W.C., Kreidenweis, S.M., 2000. Aerosol light scattering measurements as a function of relative humidity. Journal of the Air & Waste Management Association 50, 710-716.

Dick, W.D., Saxena, P., McMurry, P.H., 2000. Estimation of water uptake by organic compounds in submicron aerosols measured during the Southern Aerosol and Visibility Study. Journal of Geophysical Research 105, 1471-1479.

Draxler, R.R., 1988. Hybrid Single-Particle Lagrangian Integrated Trajectories (HYSPLIT): Model Description. NOAA Tech. Memo, ERL ARL-166, National Oceanic and Atmospheric Administration, Washington, DC.

Eldred, R.A., Cahill, T.A., Reeney, P.J., Malm, W.C., 1987. Regional patterns in particulate matter from the National Park Service network, June 1982 to May 1986, In: Bhardwaja, P.S., (Ed.) Visibility Protection, Research and Policy Aspects. Air Pollution Control Association, Pittsburgh, PA, 386-396.

Gasparini, R., Li, R., Collins, D.R., 2004. Integration of size distribution and size-resolved hygroscopicity measured during the Houston Supersite for compositional categorization of the aerosol. Atmospheric Environment 38, 3285-3303.

Gebhart, K.A., Malm, W.C., 2000. A preliminary look at source-receptor relationships in the Texas-Mexico border area. Journal of the Air and Waste Management Association 50, 858-868.

Gebhart, K.A., Kreidenweis, S.M., Malm, W.C., 2001. Back-trajectory analyses of fine particulate matter measured at Big Bend National Park in the historical database and the 1996 scoping study. The Science of the Total Environment 276, 185-204.

Hand, J.L., Kreidenweis, S.M., Sherman, D.E., Collett, J.L., Hering, S.V., Day, D.E., Malm, W.C., 2002. Aerosol size distributions and visibility estimates during the Big Bend regional aerosol and visibility observational (BRAVO) study. Atmospheric Environment 36, 5043-5055.

Jennings, S.G., O'Dowd, C.D., Cachier, H., Cooke, W.F., Sheridan, B., 1994. Volatility of elemental carbon, Journal of Geophysical Research 21, 1719-1722.

Johnson, G.R., Ristovski, Z., Morawska, L., 2004. Method for measuring the hygroscopic behavior of lower volatility fractions in an internally mixed aerosol. Journal of Aerosol Science 35, 443-455.

Knutson, E., Whitby, K., 1975. Aerosol classification by electric mobility: Apparatus, theory, and applications. Journal of Aerosol Sciences 6, 443-451.

Koontz, A.S., Flynn, C.J., Ogren, J.A., Andrews, E., Sheridan, P.J., 2003. ARM AOS Processing Status and Aerosol Intensive Properties VAP. Thirteenth ARM Science Team Meeting Proceedings, 5-7, Broomfield, CO.

Kuhns, H., Knipping, E.M., Vukovich, J.M., 2005. Development of a United States-Mexico emissions inventory for the Big Bend Regional Aerosol and Visibility Observational (BRAVO) study. Journal of Air and Waste Management Association 55, 677-692.

Kreidenweis, S.M., Remer, L.A., Bruintjes, R., Dubovik, O., 2001. Smoke aerosol from biomass burning in Mexico: Hygroscopic smoke optical model. Journal of Geophysical Research 106, 4831-4844.

Lee, T., Kreidenweis, S.M., Collett, J.L., 2004. Aerosol ion characteristics during the Big Bend Regional Aerosol and Visibility Observational Study. Journal of the Air and Waste Management Association 54, 585-592.

Lee, Y.S., Collins, D.R., Li, R., Bowman, K.P., Feingold, G., 2005. Expected impact on an aged biomass burning aerosol on cloud condensation nuclei and cloud droplet concentrations. unpublished.

Lowenthal, D.H., Kumar, N., Hand, J.L., Day, D.E., Kreidenweis, S.M., Collett, J.L., Lee, T., Ashbaugh, L., 2003. Hygroscopic aerosols during BRAVO? Journal of the Air and Waste Management Association 53, 1273-1279.

Malm, W.C., Gebhart, K.A., Henry R.C., 1990. An investigation of the dominant source regions of fine sulfur in the western United States and their areas of influence. Atmospheric Environment 24A, 3047-3060.

Malm, W.C., Sisler, J.F., Huffman, D., Eldred, R.A., Cahill, T.A., 1994. Spatial and seasonal trends in particle concentration and optical extinction in the United States. Journal of Geophysical Research 99, 1347-1370.

Malm, W.C., Day, D.E., 2000. Optical properties of aerosols at Grand Canyon National Park. Atmospheric Environment 34, 3373-3391.

Malm, W.C., Day, D.E., Kreidenweis, S.M., Collett, J.L., Lee, T., 2003. Humidity-dependent optical properties of fine particles during the Big Bend Regional Aerosol and Visibility Observational Study. Journal of Geophysical Research, 108, 4279-4294.

Markowski, G.R., 1987. Improving Twomey's algorithm for inversion of aerosol measurement data. Aerosol Science and Technology 7, 127-141.

Martin, S.T., 2000. Phase transitions of aqueous atmospheric particles. Chemical Reviews 100, 3403-3453.

Sisler, J.F., Huffman, D., Latimer, D.A., 1993. Spatial and temporal patterns and the chemical composition of the haze in the United States: An analysis of data from the IMPROVE network, 1988-1991. CIRA Report, ISSN 0737-5352-26, Colorado State University.

Sisler, J.F., Malm, W.C., Gebhart, K.A., Pitchford, M.L., 1996. Spatial and seasonal patterns and long term variability of the composition of the haze in the United States: And analysis of data from the IMPROVE network. CIRA Report, ISSN 0737-5352-32, Colorado State University.

Sloane, C.S., 1986. Effect of composition on aerosol light scattering efficiencies. Atmospheric Environment 20, 1025-1037.

Stolzenburg, M.R., 1988. An ultrafine aerosol size distribution measuring system, dissertation, Ph.D. thesis, University of Minnesota, Minneapolis, MN.

Tang, I.N., Munkelwitz, H.R., 1994. Water activities, densities, and refractive indices of aqueous sulfates and sodium nitrate droplets of atmospheric importance. Journal of Geophysical Research 99, 18,801-18,808.

Tang, I.N., Tridico, A.C., Fung, K.H., 1997. Thermodynamic and optical properties of sea salt aerosols. Journal of Geophysical Research 102, 23,269-23,275.

Twomey, S., 1965. The application of numerical filtering to the solution of integral equations encountered in indirect sensing measurements. Journal of the Franklin Institute 279, 95-109.

Twomey, S., 1975. Comparison of constrained linear inversion and an iterative nonlinear algorithm applied to indirect estimation of particle-size distributions. Journal of Computational Physics 18, 188-200.

Zhang, X.Q., McMurray, P.H., Hering, S.V., Casuccio, G.S., 1993. Mixing characteristics and water content of submicron aerosols measured in Los Angeles and at the Grand Canyon. Atmospheric Environment 27, 1593-1607.

VITA

Christopher Lee Allen was born to John and Debby Allen in Houston, Texas on April 20, 1976. While being raised in the The Woodlands, Texas, he was caught in a severe spring thunderstorm in the spring of 1986, and since numerous encounters with hurricanes and severe weather has done a lot to heighten his love for meteorology.

Christopher attended high school at McCullough High School where he was drawn to math, physics, and chemistry. Upon graduating high school Christopher decided to join the Army as a flight operation specialist. Christopher quickly moved up the ranks, garnering promotion faster than any other soldier in his unit's history. While serving in the 6th Cavalry in Korea, Christopher decided that he had served his country and was ready to take on the challenge of college. He started at Texas A&M during the spring of 1999. Christopher quickly excelled at college finishing on the deans list three times and graduated with the highest GPA in his meteorology class. During his time at A&M Christopher worked with Dr. Biggerstaff editing radar data, Dr. Nielsen-Gammon and Dr. Gary Sickler during the TEXAQS-99 project, and interned at the National Weather Service, Great Falls, MT office during the 2002 summer. He received his Bachelor of Science degree in Meteorology in 2002 and his Master of Science degree in 2005.

Christopher's research in Big Bend was funded by the Texas Commission on Environmental Quality, and is what lead to this work. He plans to remain here at A&M and continue on as a Ph.D. student under Dr. Don Collins and can be reached at: 1203B April Bloom, College Station, TX 77840.